

Banner appropriate to article type will appear here in typeset article

# Alfvén waves at low Magnetic Reynolds number

Samy Lalloz<sup>1</sup>, Laurent Davoust<sup>2</sup>, François Debray<sup>3</sup> and Alban Pothérat<sup>1†</sup>

<sup>1</sup>Coventry University, Centre for Fluid and Complex Systems, Priory Street, Coventry CV1 5FB, UK

<sup>2</sup>Grenoble-INP/CNRS/Université Grenoble-Alpes, SIMaP, Electromagnetic Processing of Materials (EPM) Laboratory, F-38000 Grenoble, France

<sup>3</sup>CNRS LNCMI, 38042 Grenoble, France

(Received xx; revised xx; accepted xx)

This paper addresses the questions whether Alfvén waves (AW) can be produced in low-magnetic Reynolds Number ( $Rm$ ) liquid metal experiments. AW are incompressible waves propagating along magnetic fields pervading electrically conducting fluids typically found in interstellar media, stellar and planetary interiors. Until now, relatively faint linear waves have been produced in liquid metals because of the large magnetic dissipation they undergo at laboratory scales (*i.e.*  $Rm \ll 1$ ) and in dense liquid metals. Thus, these questions first hinge on whether a propagative regime can be identified and whether the waves can reach sufficient amplitudes to incur nonlinearities. What is at stake, here, is the possibility of reproducing in relatively simple laboratory-scale magnetohydrodynamics (MHD) experiments some of the physical mechanisms of such far remote natural processes as anomalous heating in the solar corona, oscillations of the Earth inner core or turbulence in the solar wind.

We study AW forced by an AC electric current in a liquid metal channel pervaded by a transverse magnetic field. We first derive a wave-bearing extension of the usual low- $Rm$  MHD approximation. With it, we build a semi-analytical model for electrically-driven oscillations in a channel and identify two distinct regimes: the first one is a purely diffusive regime characterised by a sufficiently small oscillation parameter  $N_\omega$  representing the ratio of the oscillation period to the timescale of diffusive two-dimensionalisation by the Lorentz force (Sommeria & Moreau 1982). The second regime is propagative and governed by a parameter we call the *Jameson number*  $Ja$ , in an homage to the pioneering work of Jameson (1964). This number is built as the ratio of the forcing period to the timescale of AW propagation across the channel. We show that even in this regime, AW undergo significant dissipation and become dispersive as their propagation speed increases in regions of higher transversal velocity gradients. This configuration is reproduced in the FLOWCUBE experiment (Pothérat & Klein 2014), with measurements of electric potential on the top and bottom walls. Both regimes are recovered, with wave attenuation and propagation speeds in excellent agreement with the model up to  $Ja \lesssim 0.85$ . Near the  $Ja = 1$  resonance, by contrast, AW are much less attenuated and tend to propagate slower than the linear model predicts. The patterns of electric potential and dependence on the forcing amplitude confirm that this discrepancy is the signature of a nonlinear regime of AW. Hence, we show that electrically driving AW in a laboratory-scale experiment can produce all three fundamental building blocks of astro and geophysical AW: propagative, diffusive and nonlinear processes.

† Email address for correspondence: alban.potherat@coventry.ac.uk

## 1. Introduction

The main purpose of this work is to determine whether Alfvén Waves (AW) produced in liquid metal experiments can bear relevance to those in stellar or geophysical systems. Specifically, the question is whether AW can be excited and can reach sufficiently high intensity to generate complex, possibly nonlinear, dynamics despite the high dissipation they undergo.

In the absence of dissipation, AW are incompressible, non-dispersive waves propagating in electrically conducting fluids along a background magnetic field  $\mathbf{B}_0$  at a phase velocity  $V_A = B_0/\sqrt{\rho\mu}$ , where  $\rho$  is the fluid’s density and  $\mu$  the magnetic permeability of the vacuum (Roberts 1967; Moreau 1990; Davidson 2001; Finlay 2007). In a medium of finite conductivity  $\sigma$ , they dissipate over a time scale  $\tau_d = L^2/\eta$ , where  $\eta = (\sigma\mu)^{-1}$  is the magnetic diffusivity. Because of the very large scale  $L$  of stellar and geophysical systems,  $\tau_d$  is many orders of magnitude (typically 10) greater than the propagation timescale  $\tau_A = L/V_A$ . Hence, AW propagate practically unimpeded in the very low density stellar and interstellar media, the solar wind, planetary magnetospheres but also in much denser planetary interiors, where they play an important role in energy transport and dissipation (Tsurutani & Ho 1999; Nakariakov *et al.* 1999; Jault & Finlay 2015). The low dissipation favours large amplitudes and nonlinearities that underpin energy transfer between them. The solar wind offers a good example of Alfvénic turbulence, where such transfers operate across a very wide range of lengthscales (Salem *et al.* 2012; Howes 2015). In the Sun, AW are one of the candidates—reasons for the yet inexplicably high temperatures in the Solar Corona (Grant *et al.* 2018; Li *et al.* 2021). They are also commonly encountered in magnetised planetary cores, under the form of *torsional* AW propagating between concentric cylinders aligned with planets rotation (Braginsky 1970; Gillet *et al.* 2010), or as *magneto-Coriolis* waves (Finlay 2008; Gillet *et al.* 2022; Varma & Sreenivasan 2022; Majumder & Sreenivasan 2023). Unfortunately, these waves are extremely difficult to study in their natural environment. Accessibility is an obvious reason, but by no means the only one: observational data produced by satellites deliver limited local data. Furthermore, Alfvén waves compete with several other magneto-mechanical oscillations, for example incompressible oscillations of solar coronal loops, or magneto-acoustic waves arising out of the medium’s compressibility (see Nakariakov & Kolotkov (2020) for a review). Distinguishing AW amongst these, especially with limited observational data, poses a significant challenge. Numerical simulations are challenging too because of the extreme Reynolds and magnetic Reynolds numbers at which these systems operate.

For these reasons, producing carefully controlled Alfvén waves in a laboratory formed an appealing proposition to understanding their role in natural systems ever since they were first theorised by Alfvén (1942) in his seminal, yet remarkably simple paper. The immediate obstacle to such an endeavour arises from the  $10^8$  to  $10^{10}$  factor between lengthscales of experiments and natural system, which inflicts just as drastic a reduction in the ratio  $\tau_d/\tau_A$ . While higher magnetic fields linearly reduce  $\tau_A$ , even the highest magnetic fields available to date (10 T or more) ever regain 3 or 4 orders of magnitude at best. Such is the challenge of keeping this ratio sufficiently high to observe AW, that it was named after who made the first attempted (Lundquist 1949): the Lundquist number  $Lu = V_A L/\eta$ . Lundquist tried to force AW with a conducting disc oscillating across a background magnetic field in a mercury vessel and measured the intensity of these oscillations further down the field lines. The amplitude of the oscillations was weak with a frequency dependence relatively far from the non-viscous model he tried to match it to. Lehnert (1954)’s subsequent attempt was based on a similar mechanical principle. Despite improved instrumentation and control he arrived at a similar result. While Lundquist and Lehnert’s experiments set milestones as the first laboratory experiments seeking to produce AW, the most convincing evidence of AW

in liquid metals is due to [Jameson \(1964\)](#). The basis for his success was two new ideas: he showed theoretically that forcing waves electromagnetically instead of mechanically led to higher amplitudes and took advantage the spatial inhomogeneity of the waves to place his probes at the locus where a local resonance maximised their amplitude. Jameson's AW precisely matched the linear theory but, their amplitude was still too low for nonlinear effects to even be noticeable. [Alboussière \*et al.\* \(2011\)](#) tried to venture in this regime by taking advantage of electromagnets delivering up to 13 T in a 160 mm diameter bore: these authors tried to produce a self-interacting wave with an electromagnetic pulse bouncing against the ends of a vessel filled with Galinstan, and eutectic alloy liquid at room temperature. AW were produced but their decay was too fast for the reflected and incident waves to interact. Further recent experiments focused on different aspect of linear AW: [Iwai \*et al.\* \(2003\)](#) extracted the signature of AW from the pressure fluctuations. Magneto-Coriolis ([Nornberg \*et al.\* 2010](#); [Schmitt \*et al.\* 2013](#)) and torsional AW were produced more recently in liquid metal spherical Couette experiments ([Tigrine \*et al.\* 2019](#)). The most extreme AW experiment to date is without doubt owed to [Stefani \*et al.\* \(2021\)](#), who produced AW within a small capsule of rubidium subjected to a 63 T pulsed magnetic field of 150 ms. In this regime, compressibility enables these authors to excite a parametric resonance between magneto-acoustic and Alfvén waves. Although the flow was not purely incompressible, this mechanism bears relevance to those generating heat in the solar corona and this experiment is the only liquid metal experiment to have reached a nonlinear AW regime.

Independently, liquid metal MHD at laboratory scale has developed since the 1960's with the common assumption that the induced magnetic field is small enough for the magnetic induction diffusion to be several orders of magnitude greater than its advection by the flow, *i.e.* that the magnetic Reynolds number  $Rm = UL/\eta$  was vanishingly small (except where a dynamo effect was specifically sought). It became common, but potentially misleading to assume that the timescale of magnetic field fluctuations is the flow advection timescale  $L/U$ , *i.e.*  $\partial_t \mathbf{B} \sim \mathbf{u} \cdot \nabla \mathbf{B}$  ([Ennayar \*et al.\* 2021](#)). This assumption effectively merges the low- $Rm$  approximation with the Quasi-Static MHD (QSMHD) approximation, where magnetic field fluctuations are smeared out by diffusion. This led to the general belief that Alfvén waves could not exist in the limit  $Rm \rightarrow 0$ , even though early works in MHD clearly distinguished the two assumptions ([Jameson 1964](#); [Moffatt 1967](#); [Roberts 1967](#)). This context and the limited success of liquid metal experiments in producing AW led to the idea that low- $Rm$  liquid metal experiments could not produce AW of relevance to their natural settings where  $Lu \gg 1$  and  $Rm \gg 1$ . Plasmas, by contrast, soon appeared as an alternative to liquid metals due to their naturally high Lundquist numbers, especially when plasma technology for nuclear fusion emerged in the 1950's. The first indisputable evidence of AW was indeed obtained from a measure of wave velocity in a plasma ([Allen \*et al.\* 1959](#)), followed by further experiments ([Wilcox \*et al.\* 1961](#); [Jephcott & Stocker 1962](#); [Woods 1962](#)), and the generation of linear interferences between AW ([Gekelman \*et al.\* 1997](#)). The first nonlinearities in plasmas were however obtained much more recently: the observation of parametric instabilities and nonlinear transfers between AW ([Carter \*et al.\* 2006](#); [Dorfman & Carter 2016](#)) achieved an important step towards alfvénic turbulence in the lab ([Howes \*et al.\* 2012, 2013](#)). While the compressibility of plasmas makes it more difficult to isolate AW from other waves, for example magneto-acoustic waves ([Dorfman & Carter 2013](#)), it also makes them relevant to the solar corona and the solar wind. Plasmas also pose serious challenges in term of metrology and require much heavier technological environments than liquid metals. Liquid metals, by contrast are incompressible, very dense, and bear close similarities with planetary cores but current experiments with them are scarce and mostly target the linear regime.

As a result, the current state of understanding of AW is relatively limited, considering they have been discovered over 80 years ago. To this date there are no experiment reproducing

Alfvénic turbulence or able to reproduce any of the complex nonlinear effects taking place in solar or geophysical systems. Even deriving reliable laws for their reflections against walls poses considerable challenges (Schaeffer *et al.* 2012). Yet, evidence of their role in stellar and planetary interiors accumulates in simulations, and observations (Tomczyk *et al.* 2007; Gillet *et al.* 2010; Grant *et al.* 2018; Nakariakov & Kolotkov 2020; Gillet *et al.* 2022; Li *et al.* 2021; Schwaiger *et al.* 2024). A new form of Helioseismology and planetary seismology using AW is even emerging as powerful means of probing the interior of the sun and Jupiter (Hanasoge *et al.* 2012; Hori *et al.* 2023). It is also becoming increasingly clear that wherever AW play a role, they do so through dissipation and nonlinearity, rather than in a regime of ideal linear AW. In the solar corona, thin dissipation layers may be the missing heat source that could explain high temperatures there (Grant *et al.* 2018), and high dissipation occurs at small scales are energised by nonlinear transfer from larger scales (Davila 1987). In spherical shells representing planetary interiors, dissipation layers are required to obtain a correct solution describing the propagation of quasi-2D torsional AW (Luo & Jackson 2022). These examples illustrate that the regions where AW play the most crucial role are much smaller than the planetary or solar scales, so at these scales, the Local Lundquist number may fall in a range accessible to liquid metal experiments  $1 \lesssim Lu \lesssim 10^2$  (Cattell 1996; Singh & Subramanian 2007). The dissipative behaviour of liquid metal experiments may therefore not be as irrelevant to astro- and geophysical problems as the staggering values of  $Lu$  in these problems suggest. At the same time, liquid metal technology has made strides since Jameson's success: experiments (Klein & Pothérat 2010; Baker *et al.* 2018) conducted in very high magnetic fields (up to 10 T and rising) now offer extensive flow mapping based on UltraSound Velocimetry, or USV, (Brito *et al.* 2001; Franke *et al.* 2010), low-noise high-precision Electric Potential Velocimetry, or EPV (Kljukin & Thess 1998; Frank *et al.* 2001; Baker *et al.* 2017).

The role of dissipation and nonlinearities, the mounting need to understand complex AW, and the availability of these technologies prompts us to reconsider whether AW can be obtained at low- $Rm$  and sufficiently far from the QSMHD regime for AW to incur nonlinear effects. To do this, we take advantage of electric forcing and transversal homogeneity as Jameson (1964) did, and implement these ideas in high magnetic fields by adapting the FLOWCUBE device (Klein & Pothérat 2010; Pothérat & Klein 2014; Baker *et al.* 2017, 2018; Pothérat & Klein 2017), which we previously developed to study MHD turbulence. We seek to answer the following key questions:

- (i) In which conditions do AW propagate at low  $Rm$ , despite diffusion?
- (ii) How do dissipative AW differ from the ideal non-dissipative, non-dispersive AW, especially where they are not homogeneous in planes normal to the field?
- (iii) Can a nonlinear regime of AW be reached in liquid metals at low  $Rm$ ?

We first revisit the low- $Rm$  approximation, to specifically allow wave propagation, *i.e.*, outside the QSMHD regime (section 2). Based on this approximation, a semi-analytical model for the propagation of linear Alfvén waves in a plane channel normal to a background magnetic field is derived. Using this model, we analyse the flow in a channel forced by an AC current injected at a localised electrode imbedded in one of the walls, to identify the diffusive and the propagative regimes (section 3). Then, a similar flow is experimentally generated with FLOWCUBE whose principle and electric potential measurement system are summarised in section 4. By comparing theory and experiments, we finally identify the diffusive and propagative regimes in the experiment, and seek nonlinearities where discrepancies between model and experiment arise (section 5).

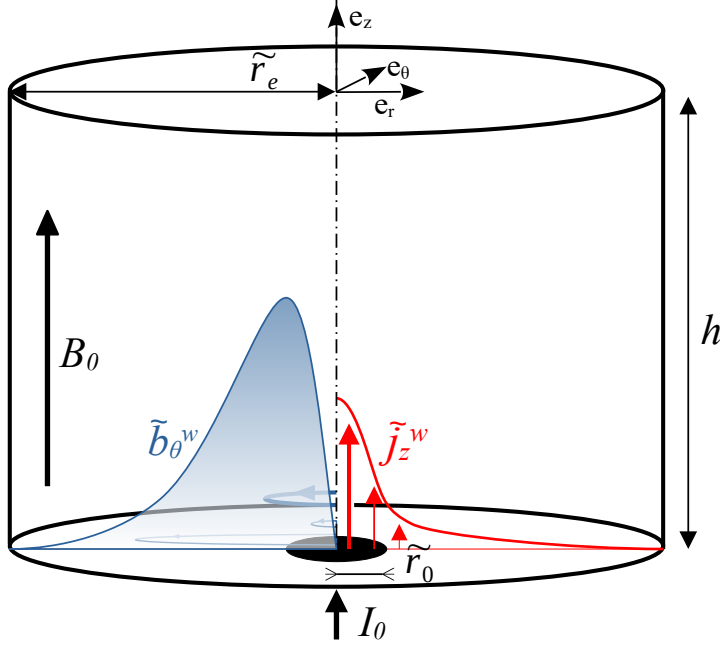


Figure 1: Sketch of the 2D axisymmetric geometry considered in the theoretical model, with a representation of the bottom boundary conditions. The right side shows the radial distribution of the axial current injected by the electrode and the left side shows the distribution of the azimuthal magnetic perturbation induced by the axial current. The black disk represents an electrode. In an experiment the total current modelled by the theoretical current distribution would be injected there. The side wall is solid, impermeable and electrically insulating.

## 2. Linear theory of confined Alfvén waves

### 2.1. General configuration and governing equations

We consider a channel of height  $h$  (figure 1) filled with an electrically conducting incompressible fluid of density  $\rho$ , kinematic viscosity  $\nu$  and electric conductivity  $\sigma$  and subjected to an axial, homogeneous and static magnetic field  $\mathbf{B}_0 = B_0 \mathbf{e}_z$ . The domain is bounded by two horizontal solid, impermeable and electrically insulating walls at  $\tilde{z} = 0$  and  $\tilde{z} = h$ , thereafter referred to as *Hartmann walls* as they are normal to the magnetic field. The flow is forced at the bottom wall by injecting an axial AC current density  $\tilde{j}_z(\tilde{r}, \tilde{z} = 0, \tilde{t}) = \tilde{j}_w(\tilde{r}) \cos(\omega \tilde{t})$  of angular frequency  $\omega$  and magnitude  $\tilde{j}_w$ . The amplitude of the total current injected at the bottom wall is  $I_0$ . Normalising distances by  $h$ , time by  $2\pi/\omega$ , velocity by  $u_0$ , magnetic fields by  $B_0$ , current density by  $j_0 = I_0/h^2$ , the governing equations for the velocity  $\mathbf{u}$ , pressure and magnetic disturbance to the external field  $\mathbf{b} = \mathbf{B} - B_0 \mathbf{e}_z$  are the Navier-Stokes equations, the induction equation, as well as the conservation of mass and magnetic flux:

$$R_\nu \partial_t \mathbf{u} + Re \{ \mathbf{u} \cdot \nabla \mathbf{u} \} = \Delta \mathbf{u} + Ha^2 Rm^{-1} \{ \partial_z \mathbf{b} + \mathbf{b} \cdot \nabla \mathbf{b} \}, \quad (2.1)$$

$$R_\eta \partial_t \mathbf{b} = \Delta \mathbf{b} - Rm \{ \mathbf{u} \cdot \nabla \mathbf{b} - \mathbf{b} \cdot \nabla \mathbf{u} - \partial_z \mathbf{u} \}, \quad (2.2)$$

$$\nabla \cdot \mathbf{u} = 0, \quad (2.3)$$

$$\nabla \cdot \mathbf{b} = 0. \quad (2.4)$$

The five non-dimensional numbers governing this system are respectively the Reynolds number, the magnetic Reynolds number, the Hartmann number and the screen parameters

for viscous and magnetic diffusion,

$$Re = \frac{u_0 h}{\nu}, \quad Rm = \frac{u_0 h}{\eta}, \quad Ha = B_0 h \sqrt{\frac{\sigma}{\rho \nu}}, \quad R_\nu = \frac{\omega h^2}{2\pi \nu}, \quad R_\eta = \frac{\omega h^2}{2\pi \eta}, \quad (2.5)$$

where  $\eta = (\sigma \mu_0)^{-1}$  is the magnetic diffusivity. Here,  $Rm$  measures the ratio of magnetic field advection by the flow to magnetic field diffusion. The square of the Hartmann number  $Ha$  measures the ratio of Lorentz to viscous forces. Finally,  $R_\nu$  (resp.  $R_\eta$ ) measures the square ratio of the viscous diffusive (resp. resistive) penetration depth of boundary oscillations into the domain to the domain's size (see for example [Batchelor \(1967\)](#)). The kinematic boundary conditions at the top and bottom Hartmann walls are no-slip impermeable:

$$\mathbf{u}(0) = \mathbf{u}(1) = 0. \quad (2.6)$$

At the bottom wall ( $z = 0$ ) the normal electric current is imposed and the top wall ( $z = 1$ ) is electrically insulating. These conditions are expressed in terms of the magnetic disturbance  $\mathbf{b}$  by means of Ampere's law,

$$\nabla \times \mathbf{b}(z = 0) \cdot \mathbf{e}_z = j_w, \quad (2.7)$$

$$\nabla \times \mathbf{b}(z = 1) \cdot \mathbf{e}_z = 0. \quad (2.8)$$

Integration in the plane of each Hartmann wall respectively leads to inhomogeneous and homogeneous conditions for  $\mathbf{b}$  at the bottom and top walls:

$$\mathbf{b}_\perp(z = 0) = \mathbf{b}_w(\mathbf{r}), \quad \mathbf{b}(z = 1) = 0, \quad (2.9)$$

where the subscript  $\perp$  stands for projection in the horizontal plane  $(x, y)$  and  $\mathbf{b}_\perp$  is uniquely defined by the choice of  $j_w(x, y)$ .

## 2.2. A propagative low- $Rm$ approximation

We start by simplifying the governing equations in the limit  $Rm \rightarrow 0$  in way suitable to describe the propagation of waves in liquid metals. In the limit  $Rm \rightarrow 0$ , the induction equation readily implies that at the leading order,

$$R_\eta \partial_t \mathbf{b} = \Delta \mathbf{b}. \quad (2.10)$$

Indeed, for the fluid motion to actually induce a magnetic field, the transport term and the magnetic diffusion must balance which implies  $\Delta \mathbf{b} = O(Rm)$  and therefore  $\mathbf{b} = O(Rm)$  ([Roberts 1967](#)). Whilst only requiring the assumption  $Rm \ll 1$ , this key result is often associated to the quasi-static MHD approximation, which carries the additional assumption that  $R_\eta \ll 1$  (in our notations). We stress, however, that this result holds regardless of any assumption made on  $R_\eta$ . In the limit  $Rm \rightarrow 0$ , the governing equations at  $O(Rm)$  and linearised in the limit of negligible inertia  $Re \rightarrow 0$  take the form:

$$(R_\nu \partial_t - \Delta) \mathbf{u} = Ha^2 \partial_z \mathbf{b}, \quad (2.11)$$

$$(R_\eta \partial_t - \Delta) \mathbf{b} = \partial_z \mathbf{u}. \quad (2.12)$$

Importantly,  $Rm$  disappears in the linearised low- $Rm$  approximation but three governing non-dimensional numbers are left: the Hartmann number  $Ha$  and the two screen parameters  $R_\eta$  and  $R_\nu$ . Eliminating either  $\mathbf{b}$  or  $\mathbf{u}$  reveals that both variables obey the same formal equation

$$\left( (R_\nu \partial_t - \Delta) (R_\eta \partial_t - \Delta) - Ha^2 \partial_{zz}^2 \right) \{\mathbf{u}, \mathbf{b}\} = 0. \quad (2.13)$$

Up to this point, boundary conditions have only been specified at the top and bottom walls, but the conditions at the lateral boundaries have remained unspecified. Let us now assume



that these allow for a solution of Eq (2.13) to be found by separation of variables under the form:

$$\{\mathbf{u}_i, \mathbf{b}_i\}(r, \theta, z) = \{\mathbf{U}_i^\perp(r, \theta) \mathbf{U}_i^z(r, \theta), \mathbf{B}_i^\perp(r, \theta) \mathbf{B}_i^z(r, \theta)\} \exp(j\epsilon t), \quad (2.14)$$

where  $\epsilon = \pm 1$ . Here,  $\mathbf{U}^\perp, \mathbf{B}^\perp, \mathbf{U}^z, \mathbf{B}^z$  are the eigenfunctions of the Sturm-Liouville problems respectively associated to the directions perpendicular and parallel with the magnetic field directions, with respective eigenvalues  $(\lambda_\perp, \lambda_z) \in \mathbb{C}^2$ :

$$(\Delta_\perp + \lambda_\perp) \{\mathbf{U}^{\lambda_\perp}, \mathbf{B}^{\lambda_\perp}\} = 0, \quad (2.15)$$

$$\left(\partial_{zz}^2 + \lambda_z\right) \{\mathbf{U}^{\lambda_z}, \mathbf{B}^{\lambda_z}\} = 0, \quad (2.16)$$

with  $\Delta_\perp = \Delta - \partial_{zz}^2$ . This decomposition leads to the dispersion relation:

$$\lambda_z^2 + \left(Ha^2 + 2\lambda_\perp + \epsilon j(R_\nu + R_\eta)\right) \lambda_z - R_\nu R_\eta + \lambda_\perp^2 + \epsilon j(R_\nu + R_\eta) \lambda_\perp = 0. \quad (2.17)$$

The boundary conditions at  $z = 0$  and  $z = 1$  impose that  $\mathbf{U}^z$  and  $\mathbf{B}^z$  are of the form  $C \exp\{(\kappa + js)z\}$ , where  $\lambda_z = (\kappa + js)^2$  incorporates real wavenumber  $\kappa$  and spatial attenuation  $s$ . The eigenvalues  $\lambda_\perp$  are determined by the geometry and boundary conditions in the horizontal plane. These are left unspecified for now, but we shall simply assume that  $\lambda_\perp = \kappa_\perp^2 > 0$  to cover the most common cases such as rectangular, periodic or axisymmetric domains. This choice enables us to introduce a real vertical wavenumber  $\kappa \in \mathbb{R}$ . Under these assumptions, the dispersion relation admits four solutions  $\lambda_{z,i} = \pm (\kappa_i + js_i)^2$ , where  $i \in \{1, 2\}$ , expressed as:

$$\kappa_i = \pm \frac{1}{2} \left[ -Ha^2 - 2\kappa_\perp^2 + \epsilon_i a + \left\{ \left( -Ha^2 - 2\kappa_\perp^2 + \epsilon_i a \right)^2 + \left( -R_\nu - R_\eta + \epsilon_i b \right)^2 \right\}^{1/2} \right]^{1/2}, \quad (2.18)$$

$$s_i = \pm \epsilon \frac{1}{2} \left[ Ha^2 + 2\kappa_\perp^2 - \epsilon_i a + \left\{ \left( -Ha^2 - 2\kappa_\perp^2 + \epsilon_i a \right)^2 + \left( -R_\nu - R_\eta + \epsilon_i b \right)^2 \right\}^{1/2} \right]^{1/2}, \quad (2.19)$$

with

$$a = \frac{1}{\sqrt{2}} \left[ Ha^4 + 4\kappa_\perp^2 Ha^2 - (R_\nu - R_\eta)^2 + \left\{ \left[ Ha^4 + 4\kappa_\perp^2 Ha^2 - (R_\nu - R_\eta)^2 \right]^2 + 4Ha^4 (R_\nu + R_\eta)^2 \right\}^{1/2} \right]^{1/2}, \quad (2.20)$$

$$b = \frac{1}{\sqrt{2}} \left[ -Ha^4 - 4\kappa_\perp^2 Ha^2 + (R_\nu - R_\eta)^2 + \left\{ \left[ Ha^4 + 4\kappa_\perp^2 Ha^2 - (R_\nu - R_\eta)^2 \right]^2 + 4Ha^4 (R_\nu + R_\eta)^2 \right\}^{1/2} \right]^{1/2}, \quad (2.21)$$

and  $\epsilon_i = (-1)^i$ . The two families of solutions  $i = 1$  and  $i = 2$  have very different damping and propagation properties. Solutions from the first family (subscript 1), decays very fast in the  $z$ -direction, as the spatial decay rate  $s_1$  is always greater than the wavenumber  $\kappa_1$ , and so the corresponding profile mostly follows an exponential decay away from the top and bottom boundaries, without achieving a complete oscillation. Physically, this mode represents the Hartmann boundary layers that develop along the bottom and top walls and we shall refer

to it as *Hartmann mode* for this reason. As such,  $s_1 \sim Ha$  in the limit  $Ha \rightarrow \infty$ , keeping  $\kappa_\perp \ll Ha$ . In contrast, solutions from the second family (subscript 2) are much less attenuated in the  $z$ -direction. Depending on the value of parameters  $Ha$  and  $\kappa_\perp$ , a range of values of  $R_\eta$  may exist such that  $s_2 < \kappa_2$ . In other words, an oscillatory solution develops into the fluid layer, which can describe the propagation of a wave. Hence, we shall refer to this mode as the *Alfvén mode*. The properties of the Alfvén mode are best illustrated in the diffusionless limit, where the acceleration term (with the time derivative) and the Lorentz force (last term of Eq. (2.13)) balance each other, as the diffusive terms become negligible compared to them. This regime is achieved in the limit where  $R_\nu \rightarrow \infty$  and  $R_\eta \rightarrow \infty$ , but keeping  $Ha^2/(R_\nu R_\eta)$  finite for the Lorentz force to remain finite. This number characterises waves driven at a specific frequency  $\omega$  such as in Lunquist, Lehnert and Jameson’s experiments. It can be expressed as the inverse of a Lundquist number based on the time scale of the oscillation instead of the magnetic diffusion timescale. However, since Jameson (1964) was the first to have successfully produced strong Alfvén waves resonances, precisely by adjusting the forcing frequency, we propose to name this number after him and define the *Jameson number* as  $Ja = (R_\eta R_\nu)^{1/2}/Ha = R_\eta/(V_A h/\eta) = R_\eta/Lu$ , where  $V_A = B_0/(\rho\mu_0)^{1/2}$  is the Alfvén velocity. Hence, in the diffusionless limit,  $Lu \rightarrow \infty$ , or equivalently, diffusion does not attenuate the propagation of Alfvén waves (Roberts 1967). Eq. (2.13) then reduces to the purely hyperbolic equation for the propagation of these waves in an ideal medium:

$$\left(\partial_{tt}^2 - Ja^{-2}\partial_{zz}^2\right)\{\mathbf{u}, \mathbf{b}\} = 0. \quad (2.22)$$

In the absence of viscous diffusion, the governing equations drop to second order and the no-slip conditions at the top and bottom boundaries need not be satisfied. For an AC injected current  $j_w$  with sinusoidal waveform, a sinusoidal wave propagates through the layer, with wavenumber found as the asymptotic value of  $\kappa_2$  in this limit:

$$\kappa_2 \sim \pm Ja = \pm \frac{(R_\eta R_\nu)^{1/2}}{Ha}. \quad (2.23)$$

Since the influence of the horizontal geometry (through  $\kappa_\perp$ ) disappears in the diffusionless limit, diffusionless Alfvén waves are non-dispersive. Hence, for a flow forced by imposing a boundary condition at one of the Hartmann walls, this boundary condition simply propagates uniformly and without dispersion along  $z$  at speed  $V_A$ . This also illustrates that the dispersive nature of the waves propagating outside the non-dissipative regime stems from the magnetic and viscous dissipation.

### 2.3. The Quasi-Static MHD limit

While the set of governing equations (2.11-2.12) potentially supports waves, it only does so when the magnetic field oscillations are not fully damped by magnetic diffusion. By contrast, the waveless regime where waves are overdamped takes place in the quasi-static (QS) limit, where magnetic diffusion acts much faster than the timescale of the variations of the induced magnetic field, i.e.  $\mu_0\sigma h^2 \ll \omega$ , or  $R_\eta \ll 1$ . As such  $|R_\eta \partial_t \mathbf{b}| \ll |\Delta \mathbf{b}|$ , so the induction equation (2.12) expresses that the magnetic field instantly adapts to the flow field. In the Navier-Stokes equation, on the other hand, since no assumption is made on  $Ha$  or  $R_\nu$ ,  $R_\nu Rm = O(Rm)$ ,  $Ha^2 \partial_z \mathbf{b} \sim Ha^2 Rm = O(Rm)$  so all terms in Eq. (2.24) are  $O(Rm)$  and must be retained. In other words, while the resistive screen parameter  $R_\eta$  must be 0 in the QS limit, the viscous screen parameter  $R_\nu$  and the Hartmann number  $Ha$  may retain finite values. Since,  $R_\nu$  remains finite whilst  $R_\eta$  vanishes, this approximation requires that  $Pm = R_\eta/R_\nu \rightarrow 0$ , and so applies to MHD flows of liquid metals or conducting electrolytes (Andreev et al. 2013; Aujogue et al. 2016; Moudjed et al. 2020) but not necessarily to plasmas. In the end, the



linearised low- $Rn$  QSMHD equations take the form

$$(R_\nu \partial_t - \Delta) \mathbf{u} = Ha^2 \partial_z \mathbf{b}, \quad (2.24)$$

$$\Delta \mathbf{b} = -\partial_z \mathbf{u}, \quad (2.25)$$

and the governing equation for  $\mathbf{u}$  and  $\mathbf{b}$  simplifies to:

$$\left( (R_\nu \partial_t - \Delta) \Delta + Ha^2 \partial_{zz}^2 \right) \{\mathbf{u}, \mathbf{b}\} = 0, \quad (2.26)$$

with the following dispersion relation

$$\lambda_z^2 + \left( Ha^2 + 2\lambda_\perp + \epsilon j R_\nu \right) \lambda_z + \epsilon j R_\nu \lambda_\perp + \lambda_\perp^2 = 0. \quad (2.27)$$

Formally, Eq. (2.26) expresses the eigenvalue problem for the dissipation operator  $\Delta - Ha^2 \Delta^{-1} \partial_{zz}^2$ , with  $\epsilon j R_\nu$  as the eigenvalue (Poth  rat & Alboussi  re 2003, 2006). The corresponding eigenfunctions offer a minimal basis for the representation of MHD flows in the QSMHD approximation (Dymkou & Poth  rat 2009; Poth  rat & Dymkou 2010; Kornet & Poth  rat 2015; Poth  rat & Kornet 2015). In the QSMHD approximation, the Lorentz force acts to diffuse momentum of transversal lengthscale  $l_\perp$  along magnetic field over distance  $l_z$  in timescale  $\tau_{2D} = (\rho/(\sigma B^2))(l_z/l_\perp)^2$ . Structures of sufficiently large scale for this process to overcome viscous dissipation and inertia become quasi-two dimensional (Sommeria & Moreau 1982; Klein & Poth  rat 2010; Poth  rat & Klein 2014; Baker *et al.* 2018). Since waves do not propagate in the quasi-static limit comparing solutions from the QSMHD equations to those the propagative low- $Rn$  equations derived in section 2.2 provides us with an effective way to detect wave propagation.

### 3. Electrically-driven waves

#### 3.1. Wave driven by injecting current with a single electrode

We now turn to the more specific case where the flow is forced by injecting electric current at one or several localised electrodes embedded in the bottom wall, which is directly relevant to the experiments. We first consider a single electrode, located at the centre of a cylindrical container of non-dimensional radius  $r_e$ . In the actual experiment, the current is fully localised within the radius of the electrode (typically 0.5 mm) and drops abruptly outside it. Mathematically, this would impose a discontinuity in  $j_w$ . To circumvent the numerical issues that would ensue, we therefore model the current injected at a single electrode located at  $r = 0$  by a sharp enough Gaussian distribution, on the basis that the impact of this change on the flow is limited, at least in the QS limit (Baker *et al.* 2015):

$$\mathbf{j}_w(r) = \frac{1}{\pi r_0^2} \exp(-(r/r_0)^2) \mathbf{e}_z, \quad (3.1)$$

where  $r_0 = \tilde{r}_0/h$  is the dimensionless radius of the electrode. The polar frame of reference  $(\mathbf{e}_r, \mathbf{e}_\theta)$  is centred on the electrode. Assuming that the magnetic perturbation is axisymmetric ( $\partial_\theta = 0$ ) and the azimuthal magnetic perturbation vanishes at  $r = 0$ , the Biot-Savart law yields the inhomogeneous Dirichlet boundary condition for the magnetic perturbation (figure 1):

$$\mathbf{b}_\perp(r, z=0, t) = b_\theta^w(r) \cos(t) \mathbf{e}_\theta = (2\pi)^{-1} \frac{1 - \exp(-r^2/r_0^2)}{r} \cos(t) \mathbf{e}_\theta. \quad (3.2)$$

In the general case, a similar condition  $\mathbf{u}_\perp(r, z = 0, t) = u_\theta^w(r, z = 0, t)\mathbf{e}_\theta$  can be imposed on the velocity at the bottom wall to force the flow with a moving wall, as [Lundquist \(1949\)](#) did experimentally. Here, for the purpose of modelling the experimental setup (see section 4), both Hartmann walls are considered as fixed, impermeable, with no slip solid walls and the top wall is assumed electrically insulated:

$$\mathbf{u}_\perp(r, z = 1, t) = \mathbf{u}_\perp(r, z = 1, t) = 0, \quad \mathbf{b}_\perp(r, z = 1, t) = 0. \quad (3.3)$$

Finally, the problem is closed with lateral boundary conditions that define the Sturm Liouville problems (2.14). Since the upper wall is electrically insulated, we assume that the current injected at the electrode escapes radially at infinity ([Baker et al. 2015](#)). Axisymmetry imposes that for  $r_e/r_0 \gg 1$ ,  $j_r \sim r^{-1}$  so the corresponding boundary condition for the Sturm-Liouville problem (2.14) is  $\lim_{r \rightarrow \infty} j_r = 0$ . Since, however we will solve the problem numerically, the boundary condition at infinity is approximated by one at finite radius  $r_e \gg r_0$ . Axisymmetric solutions of the Sturm-Liouville problems (2.14) are Bessel functions of the first kind  $J_1(\kappa_\perp^i r)$ , where  $\kappa_\perp^i$  is  $J_1$ 's  $i^{\text{th}}$  root scaled by the dimensionless radius of the vessel  $r_e$ . With these conditions in the horizontal plane, the general form for  $b_\theta$  and  $u_\theta$  takes the form

$$\{u_\theta, b_\theta\} = \sum_{i=1}^{N_\perp} \{u_\theta^i, b_\theta^i\} J_1(\kappa_\perp^i r), \quad (3.4)$$

with

$$\begin{aligned} \{u_\theta^i, b_\theta^i\}(z, t) = & \left\{ e^{s_1^i z} (\{U_1^i, B_1^i\} \cos(t + \kappa_1^i z) - \{U_2^i, B_2^i\} \sin(t + \kappa_1^i z)) \right. \\ & + e^{-s_1^i z} (\{U_3^i, B_3^i\} \cos(t - \kappa_1^i z) - \{U_4^i, B_4^i\} \sin(t - \kappa_1^i z)) \\ & + e^{s_2^i z} (\{U_5^i, B_5^i\} \cos(t + \kappa_2^i z) - \{U_6^i, B_6^i\} \sin(t + \kappa_2^i z)) \\ & \left. + e^{-s_2^i z} (\{U_7^i, B_7^i\} \cos(t - \kappa_2^i z) - \{U_8^i, B_8^i\} \sin(t - \kappa_2^i z)) \right\}. \end{aligned} \quad (3.5)$$

The real coefficients  $\{U_l^i, B_l^i\}_{l=1..8}$  are found by expanding the boundary condition (3.2) as

$$b_w(r, t) = \sum_{i=1}^{N_\perp} \left[ \frac{2}{(r_e J_2(\kappa_\perp^i r_e))^2} \int_0^{r_e} \zeta b_\theta^w(\zeta) J_1\left(\kappa_\perp^i \frac{\zeta}{r_e}\right) d\zeta \right] J_1(\kappa_\perp^i r) \cos(t). \quad (3.6)$$

From the above equation, vectors  $B_w^i$  and  $U_w^i$  are defined for each mode  $\kappa_\perp^i$  so as to express the boundary conditions on the magnetic and velocity perturbations for each term of the Bessel-Fourier series:

$$B_w^i = \frac{2}{(r_e J_2(\kappa_\perp^i r_e))^2} \int_0^{r_e} \zeta b_\theta^w(\zeta) J_1\left(\kappa_\perp^i \frac{\zeta}{r_e}\right) d\zeta [1 \ 0 \ 0 \ 0]^T, \quad (3.7)$$

with

$$U_w^i = [0 \ 0 \ 0 \ 0]^T. \quad (3.8)$$

Then, using the boundary conditions (3.7, 3.8), the linearised Navier-Stokes equation

(2.11) and Eq.(2.15, 2.16) leads to the linear system that determine  $B_l^i$  and  $U_l^i$ :

$$U_l^i = \begin{bmatrix} N_1^i & N_2^i \\ Ha^{-2} D\mathbf{z}_1^{i-1} [R_v D\mathbf{t} - M_1^i] N_1^i & Ha^{-2} D\mathbf{z}_2^{i-1} [R_v D\mathbf{t} - M_2^i] N_2^i \end{bmatrix}^{-1} \begin{bmatrix} U_w^i \\ B_w^i \end{bmatrix}, \quad (3.9)$$

$$B_l^i = Ha^{-2} \begin{bmatrix} D\mathbf{z}_1^{i-1} [R_v D\mathbf{t} - M_1^i] & 0 \\ 0 & D\mathbf{z}_2^{i-1} [R_v D\mathbf{t} - M_2^i] \end{bmatrix} U_l^i. \quad (3.10)$$

The block-arrays represent the magnetic boundary conditions, the kinematic boundary conditions and the space and time derivatives, expressed as

$$N_1^i = \begin{bmatrix} 1 & 0 & 1 & 0 \\ 0 & 1 & 0 & 1 \\ e^{s_1^i} \cos \kappa_1^i & -e^{s_1^i} \sin \kappa_1^i & e^{-s_1^i} \cos \kappa_1^i & e^{-s_1^i} \sin \kappa_1^i \\ -e^{s_1^i} \sin \kappa_1^i & -e^{s_1^i} \cos \kappa_1^i & e^{-s_1^i} \sin \kappa_1^i & -e^{-s_1^i} \cos \kappa_1^i \end{bmatrix},$$

$$N_2^i = \begin{bmatrix} 1 & 0 & 1 & 0 \\ 0 & 1 & 0 & 1 \\ e^{s_2^i} \cos \kappa_2^i & -e^{s_2^i} \sin \kappa_2^i & e^{-s_2^i} \cos \kappa_2^i & e^{-s_2^i} \sin \kappa_2^i \\ -e^{s_2^i} \sin \kappa_2^i & -e^{s_2^i} \cos \kappa_2^i & e^{-s_2^i} \sin \kappa_2^i & -e^{-s_2^i} \cos \kappa_2^i \end{bmatrix}, \quad (3.11)$$

$$D\mathbf{z}_1^i = \begin{bmatrix} s_1^i & -\kappa_1^i & 0 & 0 \\ \kappa_1^i & s_1^i & 0 & 0 \\ 0 & 0 & -s_1^i & \kappa_1^i \\ 0 & 0 & -\kappa_1^i & -s_1^i \end{bmatrix}, \quad D\mathbf{z}_2^i = \begin{bmatrix} s_2^i & -\kappa_2^i & 0 & 0 \\ \kappa_2^i & s_2^i & 0 & 0 \\ 0 & 0 & -s_2^i & \kappa_2^i \\ 0 & 0 & -\kappa_2^i & -s_2^i \end{bmatrix},$$

$$D\mathbf{t} = \begin{bmatrix} 0 & -1 & 0 & 0 \\ 1 & 0 & 0 & 0 \\ 0 & 0 & 0 & -1 \\ 0 & 0 & 1 & 0 \end{bmatrix}, \quad (3.12)$$

$$M_1^i = \begin{bmatrix} s_1^{i2} - \kappa_1^{i2} - \kappa_\perp^{i2} & -2\kappa_1^i s_1^i & 0 & 0 \\ 2\kappa_1^i s_1^i & s_1^{i2} - \kappa_1^{i2} - \kappa_\perp^{i2} & 0 & 0 \\ 0 & 0 & s_1^{i2} - \kappa_1^{i2} - \kappa_\perp^{i2} & -2\kappa_1^i s_1^i \\ 0 & 0 & 2\kappa_1^i s_1^i & s_1^{i2} - \kappa_1^{i2} - \kappa_\perp^{i2} \end{bmatrix},$$

$$M_2^i = \begin{bmatrix} s_2^{i2} - \kappa_2^{i2} - \kappa_\perp^{i2} & -2\kappa_2^i s_2^i & 0 & 0 \\ 2\kappa_2^i s_2^i & s_2^{i2} - \kappa_2^{i2} - \kappa_\perp^{i2} & 0 & 0 \\ 0 & 0 & s_2^{i2} - \kappa_2^{i2} - \kappa_\perp^{i2} & -2\kappa_2^i s_2^i \\ 0 & 0 & 2\kappa_2^i s_2^i & s_2^{i2} - \kappa_2^{i2} - \kappa_\perp^{i2} \end{bmatrix}. \quad (3.13)$$

The expressions of  $U_w^i$  and  $B_w^i$  can be easily adapted to reflect different types of electrical or mechanical forcing. For example, waves can be forced purely mechanically with an oscillatory rotation of electrically insulating top or bottom walls (or both), or electromagnetically as in the present study. Former experiments based on the generic geometry of an axisymmetric vessel subject to an axial magnetic field involve more complex types of forcing at the bottom wall: [Lundquist \(1949\)](#) mechanically forced a wave, using a disk with radial strips at the bottom of the vessel. While the actuation was mechanical and modelled as such by Lundquist, it is possible that the fluid between the strips acted as a solid electrical conductor,

whose motion induces electromagnetic forcing. [Lehnert \(1954\)](#) indeed used such indirect magnetic forcing, by driving a copper disk in oscillatory rotation, thereby inducing an axial current. Whether electromagnetic or mechanical both experiments would be modelled by a different radial distribution of velocity or magnetic field at the boundary than the one in the present study. In any case, the question of which boundary conditions best represent these two experiments remains one to clarify, as significant discrepancies exist between models and experiments.

For the purpose of modelling the present experiment, where the flow is mapped through electric potential measurements at the Hartmann walls, we need theoretical expressions for these quantities. The electric field  $\mathbf{E}$  and the electric potential gradient  $\nabla\phi$  along the transversal directions can be deduced from the magnetic and velocity fields solutions. The radial electric field  $E_r$  is directly obtained from  $u_\theta$  and  $b_\theta$  using the Ohm's law  $\mathbf{j} = \mathbf{E} + \mathbf{u} \times \mathbf{e}_z$  and Ampère's law:

$$E_r = -\partial_z b_\theta - u_\theta, \quad (3.14)$$

where the electric field is normalized by  $E_0 = \sigma u_0 B_0$ . Defining coefficients  $E_l^i$  for the electric field in the same way as  $U_l^i$  and  $B_l^i$ , these satisfy:

$$E_l^i = -U_l^i - \begin{bmatrix} Dz_1^i & 0 \\ 0 & Dz_2^i \end{bmatrix} B_l^i. \quad (3.15)$$

The electric potential gradient is directly measured experimentally, and related to the magnetic vector potential  $\mathbf{A}$ , where  $\mathbf{b} = \nabla \times \mathbf{A}$  through Faraday's law, and Coulomb's gauge  $\nabla \cdot \mathbf{A} = 0$ :

$$-\partial_r \phi = E_r + \partial_t A_r \quad (3.16)$$

$$\Delta A_r = -\partial_z b_\theta. \quad (3.17)$$

Defining coefficients  $\Phi_l^i$  for  $\partial_r \phi$  as before, we finally obtain:

$$\Phi_l^i = - \begin{bmatrix} Dz_1^i - DtM_1^{i-1} Dz_1^i & 0 \\ 0 & Dz_2^i - DtM_2^{i-1} Dz_2^i \end{bmatrix} B_l^i - U_l^i. \quad (3.18)$$

From these coefficients, the radial potential gradient is expressed as

$$\partial_r \phi(r, z, t) = \sum_{i=1}^{N_\perp} \partial_r \phi^i(z, t) J_1(\kappa_\perp^i r), \quad (3.19)$$

with

$$\begin{aligned} \partial_r \phi^i(z, t) = & \left\{ e^{s_1^i z} (\Phi_1^i \cos(t + \kappa_1^i z) - \Phi_2^i \sin(t + \kappa_1^i z)) \right. \\ & + e^{-s_1^i z} (\Phi_3^i \cos(t - \kappa_1^i z) - \Phi_4^i \sin(t - \kappa_1^i z)) \\ & + e^{s_2^i z} (\Phi_5^i \cos(t + \kappa_2^i z) - \Phi_6^i \sin(t + \kappa_2^i z)) \\ & \left. + e^{-s_2^i z} (\Phi_7^i \cos(t - \kappa_2^i z) - \Phi_8^i \sin(t - \kappa_2^i z)) \right\}. \end{aligned} \quad (3.20)$$

Using the same procedure, the QSMHD solution is obtained for each set of parameters  $Ha$ ,  $R_v$ ,  $R_\eta$  using Eq. (2.3) instead of Eq. (2.2).

### 3.2. Quantities for flow diagnosis

Being now in a position to express solutions semi-analytically, we define three quantities -represented schematically in figure 2- to best characterise how oscillations imposed at the bottom wall propagate, damp and rotate across the layer, in both theory and experiments:

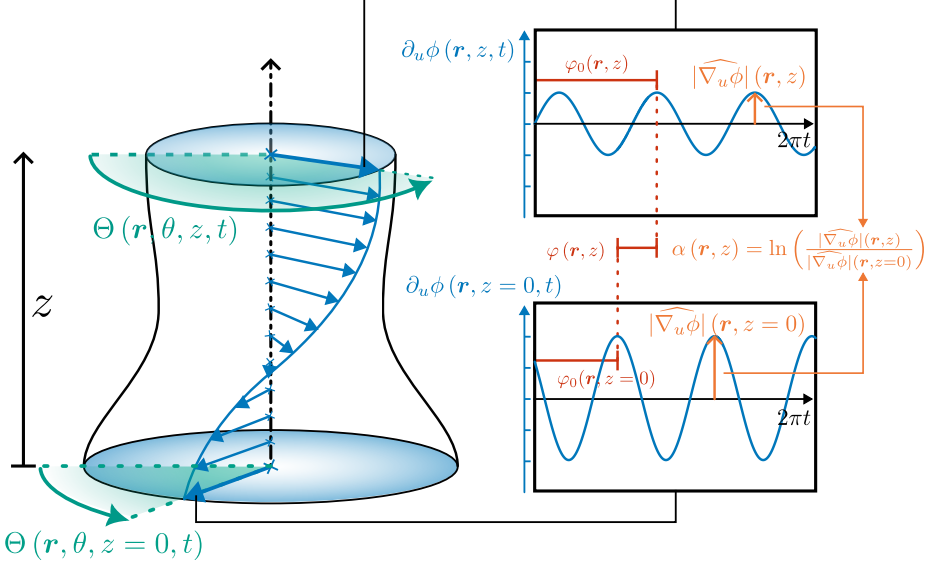


Figure 2: Illustration of the different diagnosis quantities for the oscillating flow: the local phase shift  $\varphi(r, z) = \varphi_0(r, z) - \varphi_0(r, z=0)$ , the local attenuation coefficient  $\alpha(r, z) = \ln \left( \frac{|\widehat{\nabla_u \phi}|(r, z)}{|\widehat{\nabla_u \phi}|(r, z=0)} \right)$  and the horizontal polar angle  $\Theta(r, \theta, z, t)$  of the electric potential gradient  $\nabla \phi$ .

- The local phase shift with respect to the bottom wall, at  $(r, z) = (x, y, z)$ , based on electric potential gradients along a horizontal unit vector  $\hat{e}_u$  (thereafter  $\mathbf{e}_r$  or  $\mathbf{e}_x$ ):

$$\varphi(r, z) = \varphi_0(r, z) - \varphi_0(r, z=0), \quad (3.21)$$

where  $\varphi_0(r, z) = \arg \left\{ \int_{-\infty}^{\infty} \mathbf{e}_r \cdot \hat{e}_u \cdot \nabla \phi(r, z, t) e^{-jt} dt \right\}$  is the phase of  $\partial_u \phi$ , obtained analytically from Eq. (3.19).

- The local attenuation coefficient for  $\partial_u \phi$ :

$$\alpha(r, z) = \ln \left( \frac{|\widehat{\nabla_u \phi}|(r, z)}{|\widehat{\nabla_u \phi}|(r, z=0)} \right), \quad (3.22)$$

where  $|\widehat{\nabla_u \phi}|(r, z) = 2 \left| \int_{-\infty}^{\infty} \hat{e}_u \cdot \nabla \phi(r, z, t) e^{-jt} dt \right|$  is the amplitude of the oscillation of  $\partial_r \phi$  at unit angular frequency (dimensionally  $\omega$ ), also calculated analytically from Eq. (3.19).

- The horizontal polar angle  $\Theta$  of  $\nabla \phi$  with respect to the origin

$$\Theta(r, \theta, z, t) = -\arctan \left( \frac{\sin \theta \mathbf{e}_r \cdot \nabla \phi(r, z, t) + \cos \theta \mathbf{e}_\theta \cdot \nabla \phi(r, z, t)}{\cos \theta \mathbf{e}_r \cdot \nabla \phi(r, z, t) - \sin \theta \mathbf{e}_\theta \cdot \nabla \phi(r, z, t)} \right). \quad (3.23)$$

The first two quantities are defined so as to return the spatial attenuation and phase shift of a pure sinusoidal planar wave of the form  $\exp(\alpha z) \sin(\kappa z - \omega t)$ . For axisymmetric flows,  $\Theta$  reduces to  $\theta$  and thus is not of interest, but will come in hand in section 4, where the flow is forced with four electrodes and thus no longer axisymmetric.

### 3.3. Numerical solver

An in-house Matlab code was developed to numerically solve the axisymmetric one-electrode problem, *i.e.* to evaluate time-dependent fields  $u_\theta$ ,  $b_\theta$ ,  $E_r$ ,  $\partial_r \phi$  and  $E_r$  on a discrete grid. The code first solves for  $s_i, \kappa_{zi}$  in (2.18) and (2.19) and then solves the  $N_\perp$  systems of 16 equations (3.9-3.10) to determine coefficients  $U_l^i$  and  $B_l^i$ . Because  $|s_i|$  and  $\kappa_l$  scale with  $Ha$  and appear as exponential arguments, the variable-precision arithmetic package in Matlab was used to ensure a sufficient accuracy in computing the solutions, with the number of digits set to 320. The code takes as input  $R_\eta$ ,  $R_v$  and  $Ha$ , the radial location  $r$ , the number of transverse modes  $N_{\kappa_\perp}$ , the outer radius  $r_e$  and the requested time-interval for evolution.

The discretisation in time and in the  $z$  direction are for display only and do not affect the precision of the result. Similarly the precision of the solution for each mode  $\kappa_\perp^i$  depends only on the numerical precision set. On the other hand, the approximation of the boundary condition from a Fourier-Bessel expansion leads to two errors: First, the finite number of modes in the series  $N_\perp$  incurs a discretisation error. Second, an error on current conservation appears by setting boundary condition  $J_r = 0$  at a finite radius  $r_e$  instead of infinity. We assess both type errors relative to a high resolution run at  $N_\perp^{\max} = 2500$  for  $r_e = \{0.66, 1.32, 2.65\}$  respectively as:

$$\varepsilon(r_e, N_{\kappa_\perp}) = \frac{\| \partial_r \phi(N_{\kappa_\perp}) - \partial_r \phi(N_{\kappa_\perp}^{\max}) \|}{\| \partial_r \phi(N_{\kappa_\perp}^{\max}) \|}, \quad (3.24)$$

and

$$\varepsilon_b(r_e) = \frac{\| b_w(r, t=0, r_e) - b_\theta^w \|}{\| b_\theta^w \|}, \quad (3.25)$$

where  $\| \cdot \|$  represents the  $\mathcal{L}^2$  norm. Convergence tests performed with the propagative low- $Rm$  model show that  $\varepsilon_b \sim r_e^{-2}$  for  $r_e \gtrsim 0.6$  and  $\varepsilon \sim N_\perp^{-54}$  for the sets  $\{N_\perp \gtrsim 10^3, r_e = 2.65\}$  and  $\{N_\perp \gtrsim 600, r_e = 1.34\}$ . Based on this result, a good compromise between numerical cost and precision is reached by setting  $r_e$  and  $N_\perp$  so as to ensure  $\varepsilon_b \leq 1\%$  on  $b_w$  for any  $r$ , and  $\varepsilon \leq 10^{-10}$  for all forthcoming calculations. The same test is conducted on the QSMHD model, with similar results, so that forthcoming comparison between the two models are conducted with the same number of modes  $N_\perp$ .

### 3.4. Propagative resonance versus oscillating diffusive maxima

We first seek to identify the parameter regimes where propagation occurs and the purely diffusive ones. To this end, we seek solutions of the one-electrode problem with both the propagative low- $Rm$  model and the QSMHD model which cannot produce waves for  $Ha \in \{2.23, 2.66, 3.18, 3.80\} \times 10^4$  and  $R_\eta \in [4.3 \times 10^{-5}, 5.1 \times 10^1]$ . These values are chosen to match the experimentally accessible range. Waves are expected where discrepancies exist between the models. Figure 3 represents the variations of the attenuation coefficient  $\alpha$  ( $r = 0.1, z = 1$ ) with  $R_\eta$ , renormalised with two different parameters designed to highlight the purely diffusive regime and the propagative regime respectively.

The first parameter  $N_\omega = Ha^2/R_v$  represents the ratio between the Lorentz force and the acceleration term, present in both models. As such, it does not account for propagative phenomena. We call it *oscillation parameter* by analogy with the interaction parameter that measures the ratio of Lorentz force to the inertial terms in QSMHD (Moreau 1990). The solutions of the QSMHD and the propagative Low- $Rm$  models collapse for all  $Ha$  numbers in the limit  $N_\omega \rightarrow 0$  and exhibit a maximum value at  $N_\omega^{-1} = 1 \times 10^{-3}$ . As such this maximum does not stem from propagative phenomena. The solution of both models starts to diverge around this maximum (marked (1a-1d) on figure 3), with a relative error from 3% to 10% for  $2.23 \times 10^4 \leq Ha \leq 3.18 \times 10^4$ . The two models diverge much more



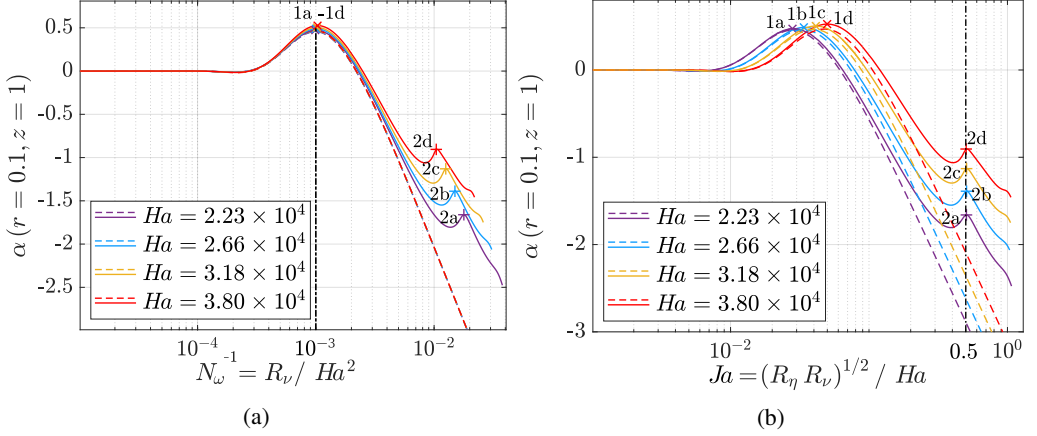


Figure 3:  $\alpha$  against  $N_\omega^{-1}$  (a) and  $Ja$  (b) for  $Ha = \{1.9 \times 10^4, 2.66 \times 10^4, 3.18 \times 10^4, 3.8 \times 10^4\}$ . Solid lines (—): propagative low- $Rn$  model, dashed lines (---): QSMHD model. Calculations are performed at  $r = 0.1$ . The attenuation coefficient  $\alpha$  is calculated at  $z = 1$ .

significantly around a second set of maxima (marked (2a-2d) on figure 3), that only exists in the propagative solution. As such, this second set of maxima necessarily results from a propagative process. On figure 3b, the attenuation coefficients are plotted against the Jameson number  $Ja = (R_\eta R_\nu)^{1/2} / Ha$ . All maxima from the second set (2a-2d) collapse at the same value of  $Ja = 0.5$ , for all Hartmann numbers. Dimensionally, the period associated with these maxima therefore scales with the propagation time of Alfvén waves across the channel, and so suggests a form of resonance due to Alfvén waves.

Hence two maxima corresponds to reduced attenuation of the oscillations across the channel: one is purely diffusive (henceforth referred to as *oscillating-diffusive*), and the other one is due to Alfvén wave resonances (henceforth *propagative*). To understand the precise mechanism behind each of them, we now inspect the spatial distribution of the local amplitude  $|\widehat{\nabla_r \phi}|$ , the attenuation  $\alpha(r, z)$  and the phase  $\varphi(r, z)$  of the electric potential gradients. Solutions from the QSMHD and propagative low- $Rn$  models are represented on figures 4, 5 and 6 for different values of the Jameson numbers  $Ja = 0.25$  (a,e), 0.5 (b,f), 0.75 (c,g) and 1 (d,h).

### 3.5. Phenomenology of the oscillating diffusive maxima

Understanding the mechanism underpinning the oscillating diffusive maxima requires a closer look at the region near  $r = 0$ , where velocities are small. Since in the limit  $r \rightarrow \infty$ ,  $\mathbf{u} \rightarrow 0$ , the flow reaches a maximum velocity at a radius  $r_m$  between the close and far regions, also visible on the profiles of electric potential gradients from figure 4. The fluid is accelerated in the region  $r \leq r_m(z)$ . In the limit  $R_\nu \rightarrow 0$ , this region is governed by the balance between viscous friction in horizontal planes and the Lorentz forces:

$$\nu \Delta_\perp \sim \nu Ha^2 \Delta_\perp^{-1} \partial_{zz}^2, \quad (3.26)$$

which, for a lengthscale along  $z$  scaling with  $z$ , leads to the classical scaling for the thickness of vortex cores in high magnetic fields:  $\tilde{r}_m^{(\nu)} \sim h Ha^{-1/2} (\tilde{z}/h)^{1/2}$ . Crucially, the vortex core becomes thicker as the axial distance to the injection point increases (Sommeria 1988).

For  $R_\nu$  sufficiently large, the acceleration term  $\partial_t$  overcomes viscous friction to balance the Lorentz force and so  $\tilde{r}_m^{(\omega)}(\tilde{z}) \sim h (Ha^2 / R_\nu)^{-1/2} \tilde{z}/h = N_\omega^{-1/2} \tilde{z}/h$ . The transition between

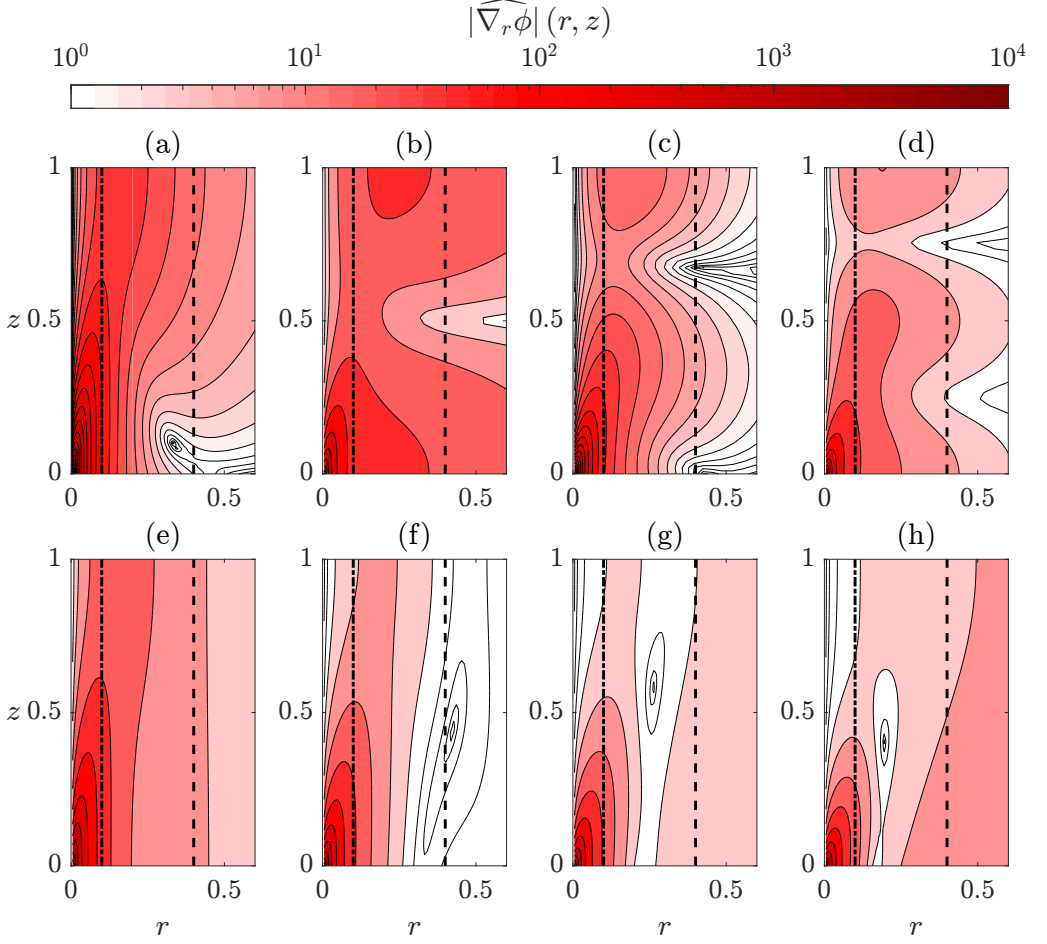


Figure 4: Contours of  $|\widehat{\nabla_r \phi}|$  at  $Ha = 3.8 \times 10^4$  and for  $Ja = \{0.25$  (a,e);  $0.5$  (b,f);  $0.75$  (c,g);  $1$  (d,h) $\}$ , (a-d) propagative low- $Rm$  model, (e-h) QSMHD model. The vertical dash-dotted line ( $-\cdot-\cdot-$ ) is located at  $r = 0.1$  and the vertical dashed line ( $- - -$ ) at  $r = 0.4$ .

these two regimes takes place when  $\tilde{r}_m^{(\omega)} \sim \tilde{r}_m^{(\nu)}$ , *i.e.* when  $R_\nu \sim Ha$  at  $\tilde{z} = h$ . Since the oscillating diffusive maximum is located at  $R_\nu/Ha = Ha N_\omega^{-1} \gtrsim 10 \gg 1$  for all values of  $Ha$  considered, it is well within the regime dominated by the oscillating term. In this regime too, the vortex core becomes wider at larger distance from the electrode. However, when  $z$  reaches the axial wavelength of the oscillations  $2\pi/\kappa$ , the second derivative  $\partial_{zz}$  saturates (at  $(\tilde{\kappa})^2/(4\pi^2)$ ) and so does the radius of the vortex core. This  $z$ -variation implies that the point  $r = \tilde{r}/h = 0.1$  on the bottom wall is always outside of the region where oscillations are strong, whereas for  $\tilde{r} > \tilde{r}_m$ , the point  $r = 0.1$  on the top wall is inside it. Hence, when  $R_\nu$  varies from 0, the ratio of amplitudes of the oscillations at the top and bottom is the highest when  $\tilde{r}_m^{(\omega)}$  coincides with the location of the probe  $r = 0.1$ , and so explains the existence of the oscillating diffusive maxima. The contours plots of  $|\widehat{\nabla_r \phi}|$  in figure 7 obtained with the QSMHD model for three different  $N_\omega$  values, *i.e.*  $N_\omega = \{0.75, 1, 1.25\} \times 10^{-3}$ , illustrate these effect and that the vortex radius at the top plate increases with  $N_\omega^{-1}$ .

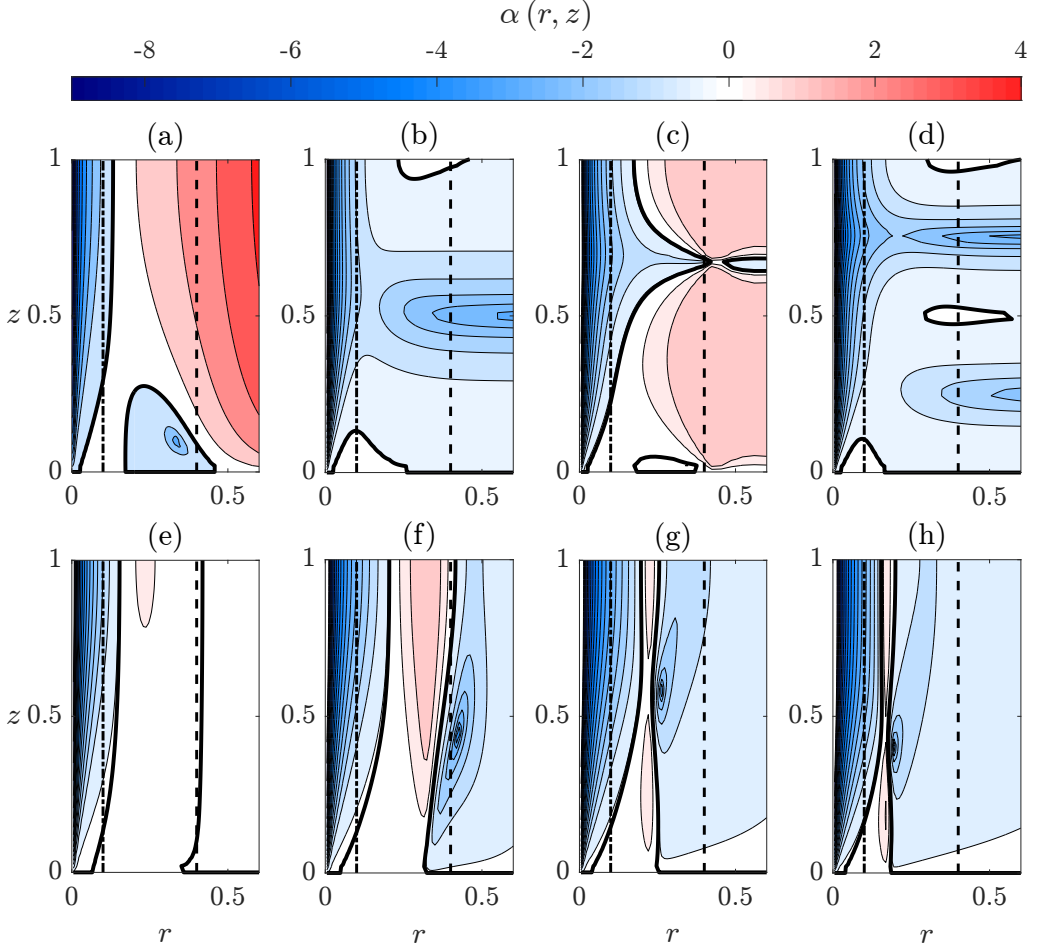


Figure 5: Contours of  $\alpha(r, z)$  at  $Ha = 3.8 \times 10^4$  and for  $Ja = \{0.25 \text{ (a,e); } 0.5 \text{ (b,f); } 0.75 \text{ (c,g); } 1 \text{ (d,h)}\}$ , (a-d) propagative low- $Rn$  model, (e-f) QSMHD model (e-f). The vertical dash-dotted line ( $-\cdot-\cdot-$ ), indicates the radial position  $r = 0.1$  where values of  $\alpha$  are taken for figure 3. The solid line ( $—$ ) is the locus of  $\alpha(r, z) = 0$ .

### 3.6. Phenomenology of the propagative maxima

The propagative resonance is governed by the reflection of Alfvén waves on the Hartmann walls, as each propagative resonance corresponds to values of  $R_\eta$  (or of the frequency) for which the wavelength  $l_A = V_A/2\pi\omega$  is an integer fraction of the channel height  $h$  or, equivalently,  $Ja = \{1/4, 1/2, 3/4, 1\ldots\}$ .

Far from the electrode, the radial velocity and potential gradients are small compared to the axial ones. This is made visible through the horizontal orientation of  $\varphi$  isolines as  $r$  increases (figure 6). In areas of low radial gradient, such as near  $r = 0.4$ , propagative resonances appear at  $Ja = \{1/4, 3/4\}$  *i.e.* respectively  $l_A = \{1h/4, 3h/4\}$ . This is illustrated on figure 8, which shows the variations of  $\alpha$  with  $Ja$  for two radial locations  $r = \{0.1, 0.4\}$  at  $Ha = 3.8 \times 10^4$ . The maximum in  $\alpha$  results from the co-existence of a minimum of  $|\widehat{\nabla_r \phi}|$  at the bottom wall and a maximum at the top wall. This is also visible from the location of the node and anti-node of  $|\widehat{\nabla_r \phi}|$  along the dashed line ( $---$ )  $r = 0.4$  in figures 4b and 4c. This case corresponds to theory and observations of Jameson (1964), whose resonances also appears

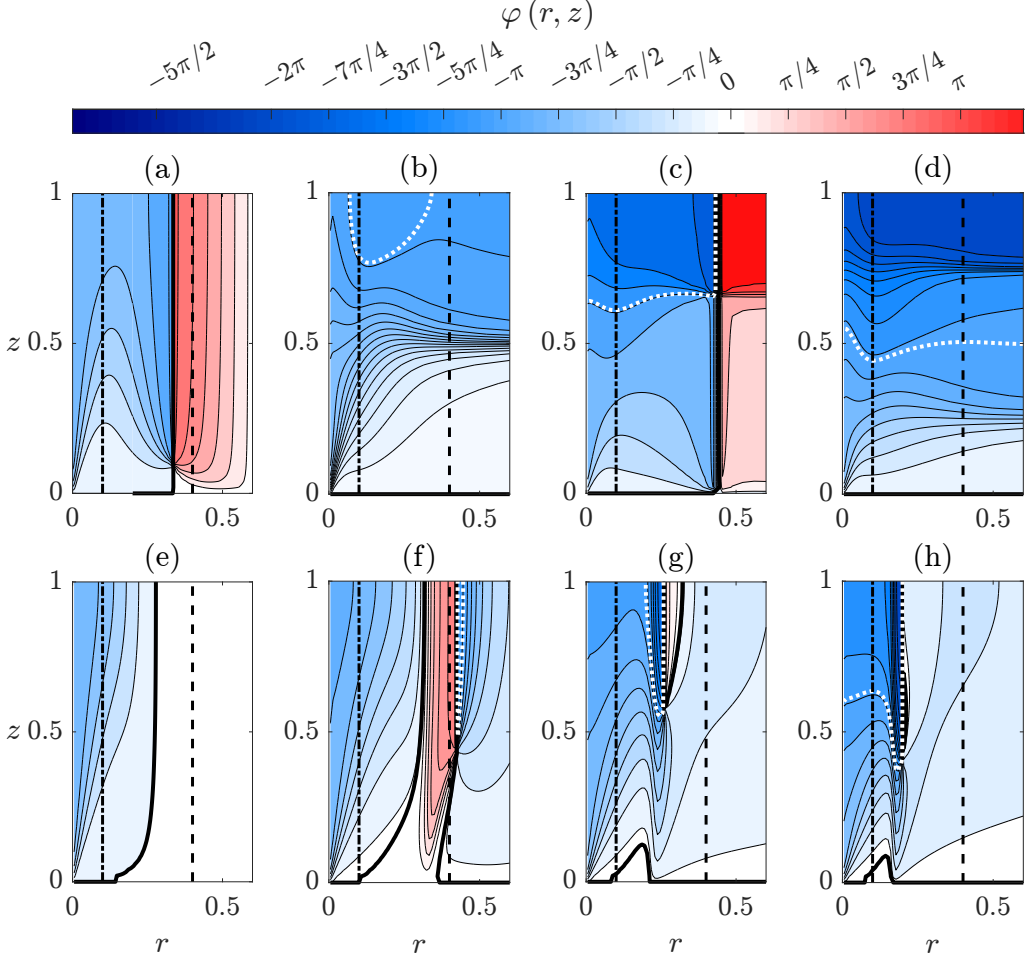


Figure 6: Contours of  $\varphi$  at  $Ha = 3.8 \times 10^4$  and for  $Ja = \{0.25 \text{ (a,e); } 0.5 \text{ (b,f); } 0.75 \text{ (c,g); } 1 \text{ (d,h)}\}$ : (a-d) propagative low- $Rn$  model, (e-h) QSMHD model. The solid line (—) marks the  $\varphi = 0$  iso-value and the dotted line (.....) the  $\varphi = -\pi$  iso-value.

at  $Ja = 1/4$  and  $3/4$ , in our notations. Close to the electrode, by contrast, radial gradients increase significantly. Comparing the values of  $\alpha$  at  $r = 0.1$  with those at  $r = 0.4$  in figure 5, shows that the attenuation coefficient decreases in absolute value in this region. Hence waves are more strongly damped in areas of higher transversal gradients, because of the extra Joule dissipation that these incur. In this region, e.g. at  $r = 0.1$ , the propagative resonance appears at  $Ja = 0.5$  (marked (2a-2d) on figure 3b). Plots of  $\varphi$  against  $Ja$  at  $r = 0.1$  for different values of  $Ha$  on figure 9 reveal that the phase shift between the two Hartmann walls is  $-\pi$  at this resonance. Thus, propagative resonances in strong radial gradients take place in phase opposition, which is confirmed by the two anti nodes of  $|\widehat{\nabla_r \phi}|$  located at the Hartmann walls for this  $Ja$  value (see figure 4b).

Lastly, an ideal AW propagating between the Hartmann walls would incur a phase shift with a linear dependence on  $Ja$ . From figure 9, by contrast,  $\varphi$  exhibits a nonlinear dependence on  $Ja$ . The discrepancy to linearity is particularly pronounced when  $Ja \lesssim 0.8$ . This regime overlaps the regime of wave propagation for  $Ja \gtrsim 0.1$ , so in this regime, dissipation causes AW to become dispersive. This effect however progressively vanishes at higher values of

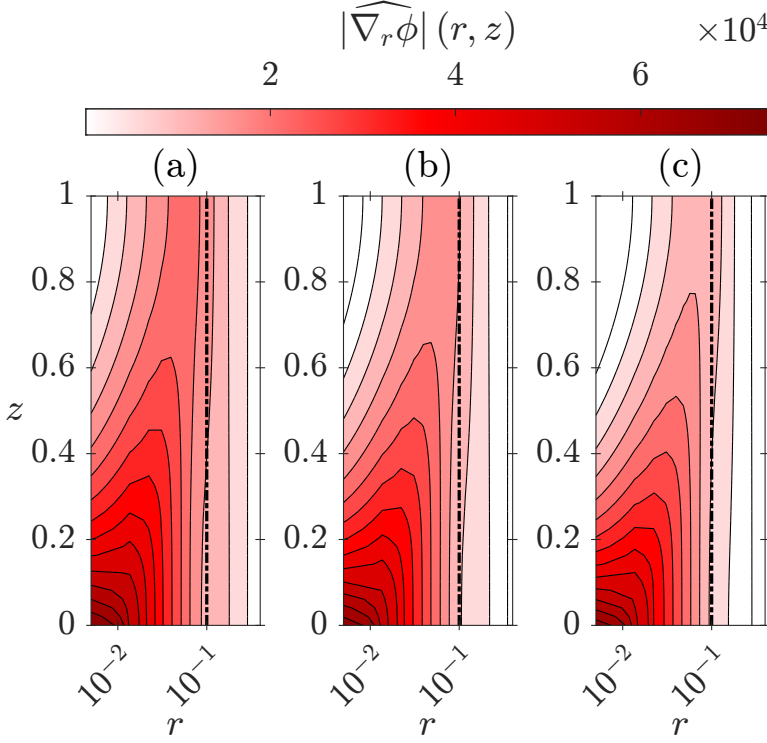


Figure 7: Contours of  $|\widehat{\nabla_r \phi}|$  from the QSMHD model at  $Ha = 3.8 \times 10^4$  and for  $N_\omega^{-1} = \{0.75 \text{ (a), } 1 \text{ (b), } 1.25 \text{ (c)}\} \times 10^{-3}$ .

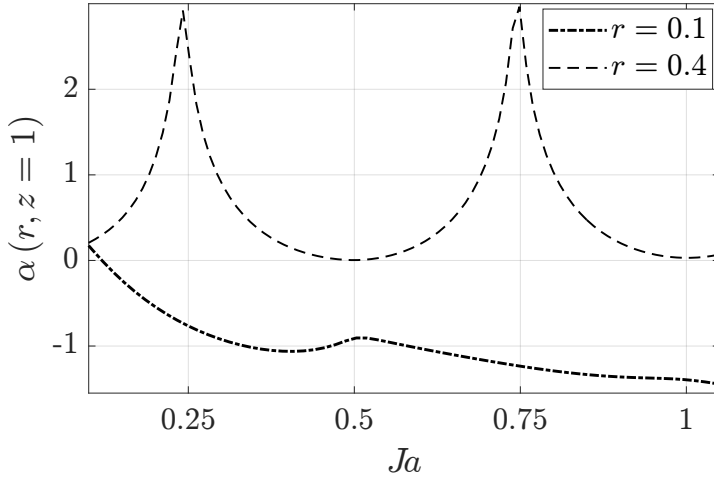


Figure 8:  $\alpha$  from the propagative low- $Rn$  model against  $Ja$  for  $r = \{0.1, 0.4\}$  at  $Ha = 3.8 \times 10^4$ .

$Ja$ . Hence, in this limit, a nearly dispersionless propagative regime is recovered, despite the dissipation.

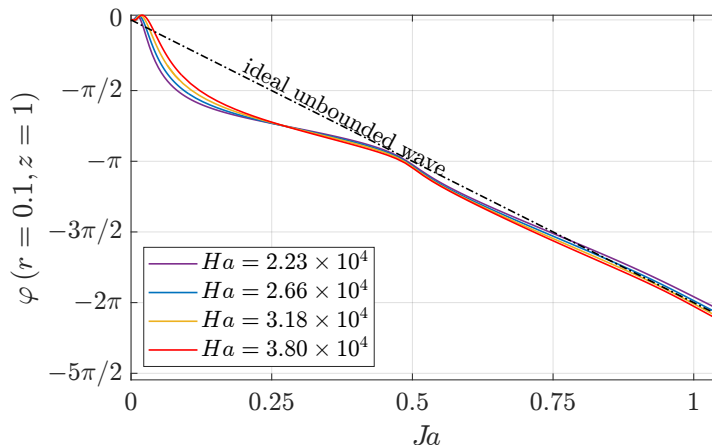


Figure 9:  $\varphi$  from the propagative low- $Rn$  model against  $Ja$  at  $r = 0.1$  for  $Ha = \{1.9 \times 10^4, 2.66 \times 10^4, 3.18 \times 10^4, 3.8 \times 10^4\}$ . The dash-dotted line (---)  $\varphi$  is for an ideal unbounded wave.

## 4. Experimental methods

### 4.1. The FLOWCUBE experimental device

The experimental device is an upgraded version of the FLOWCUBE facility (Klein & Poth  rat 2010; Poth  rat & Klein 2014; Baker *et al.* 2017). It consists of a modular cuboid vessel of inner height  $h = 10$  cm and width  $L = 15$  cm. The side walls are electrically insulated and made of polycarbonate. The top and bottom Hartmann walls in contact with the fluid are printed circuit boards (PCBs) made of an FR4 epoxy layer and a ROGER 4003 ceramic layer acting as an insulator, all mounted on polyamide-coated brass frame. Both are fitted with injection electrodes to drive the flow, and probes to measure electric potentials. The working liquid metal hermetically enclosed inside the vessel is an eutectic alloy of gallium, indium and tin that is liquid at room temperature, of electric conductivity  $\sigma = 3.4 \times 10^6$  S/m, density  $\rho = 6400$  kg m<sup>-3</sup>, kinematic viscosity  $\nu = 3.7 \times 10^{-7}$  m<sup>2</sup> s<sup>-1</sup> (*i.e.* that the magnetic Prandtl number  $Pm = R_\eta/R_\nu = \nu/\eta = 1.6 \times 10^{-6}$ ). The procedures described in Baker *et al.* (2017) ensure hermetic filling of and good electrical contact between the metal and both set of probes and electrodes. FLOWCUBE is subjected to a static and uniform axial magnetic field  $B_0 e_z$  provided by the 12 MW M10 resistive electromagnet of 376 mm diameter bore at the LNCMI (CNRS) in Grenoble. The field homogeneity over the vessel is about 5%. The range of magnetic fields used  $B_0 = \{5.87, 7, 8.37, 10\}$  T corresponds to Hartmann numbers  $Ha = \{1.9 \times 10^4, 2.66 \times 10^4, 3.18 \times 10^4, 3.8 \times 10^4\}$ .

### 4.2. Flow forcing mechanism

As in Sommeria (1986), Klein *et al.* (2009) and Baker *et al.* (2017), the flow is driven by injecting a prescribed current through an array of electrodes fitted flush at the bottom Hartmann wall located at  $z = 0$ . These are arranged on a 16x16 square lattice spaced 5 mm apart and a ring lattice of 8 electrodes per side spaced 15 mm apart (figure 10). Each of the electrodes is made of 1 mm diameter copper wire and surface-coated with a thin layer of gold to warrant the electrical contact with the liquid metal. An AC electric current is injected through a subset of these electrodes. In this paper, the corresponding forcing pattern is a near-central square of  $2 \times 2$  electrodes spaced by  $\tilde{d}_0 = 0.02$  m (non-dimensionally,  $d_0 = \tilde{d}_0/h = 0.2$ ), with adjacent electrodes of opposite polarities (figure 10). The injected current is generated by a HP 33120A function generator feeding into two



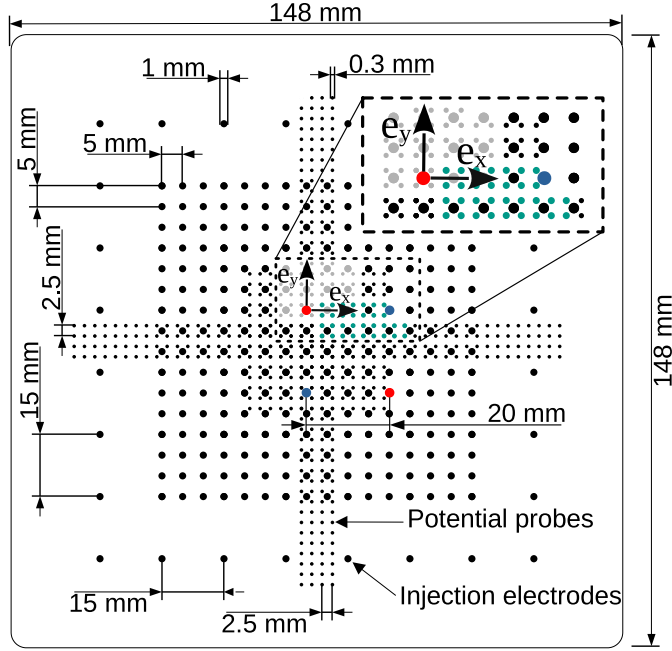


Figure 10: Sketch of the face of the bottom Hartmann wall in contact with the GaInTn alloy. The injection pattern used during the experiments is represented by coloured circles. The red circles are connected to the phase of the AC power supply and the blue ones to the neutral. The blue and red electrodes are in phase opposition. Tail circles represent active potential probes.

superimposed KEPCO 400 W BOP 20-20M amplifiers. It is sinusoidal, with a frequency range  $\omega/(2\pi) \in [1, 1330]$  Hz corresponding to  $R_\eta \in [4.4 \times 10^{-2}, 5.8 \times 10^1]$ . Different RMS current intensities  $|I_0|$  per electrode were investigated, from 0.1 A to 6.5 A per electrode. To overcome current variations incurred by fluctuations in the contact resistance between metal and electrodes (of the order of  $1 \times 10^{-2} \Omega$ ), a constant ohmic resistance of  $2 \Omega \pm 0.25\%$  is added in series to each electrode (Pothérat & Klein 2014). Injecting AC current in this way drives an oscillatory flow of controlled frequency, amplitude, and transversal lengthscale given by the pitch  $\bar{d}_0$  between electrodes.

#### 4.3. Measurement of electrical potentials

The flow is diagnosed using two arrays of electric potential probes fitted flush at the surface of each Hartmann wall. They are arranged on a 2.5 mm lattice made of a central square of  $14 \times 14$  probes, and two perpendicular arrays of  $4 \times 48$  probes spanning the  $x$  and  $y$  directions of the Hartmann walls (figure 10). The arrays of both walls are aligned opposite each other along  $\mathbf{e}_z$ . Additionally one of four potential probes located at the outer ring of the wall serves as reference for potential measurements. Each potential probe is made of 0.2 mm diameter copper wire touching the metal at the wall surface. From these potential probes, the electric signals are gathered through PCBs embedded into the Hartmann walls and routed externally to two National Instrument PXIe-4303 data acquisition modules housed in a PXI express chassis clocked at 10 MHz. Each module synchronously records the signals of 32 probes to 24-bit precision at a sampling frequency of up to 52.2 kHz per channel, with a low RMS noise ( $3.2 \mu V$ ). Such high acquisition frequencies are required to accurately capture phase shift between the Hartmann walls of oscillations expected to fall into either the oscillating

|                          |                       |                       |                       |                       |
|--------------------------|-----------------------|-----------------------|-----------------------|-----------------------|
| $B_0$ [T]                | 5.87                  | 7                     | 8.37                  | 10                    |
| $\omega_{min}/2\pi$ [Hz] | 1                     | 1                     | 1                     | 1                     |
| $\omega_{max}/2\pi$ [Hz] | 781                   | 933                   | 1115                  | 1330                  |
| $I_0$ [Arms]             | 1.40                  | 1.40                  | 1.40                  | 1.40                  |
| $Ha$                     | $2.23 \times 10^4$    | $2.66 \times 10^4$    | $3.18 \times 10^4$    | $3.80 \times 10^4$    |
| $R_{\eta min}$           | $4.36 \times 10^{-2}$ | $4.36 \times 10^{-2}$ | $4.36 \times 10^{-2}$ | $4.36 \times 10^{-2}$ |
| $R_{\eta max}$           | $3.41 \times 10^1$    | $4.07 \times 10^1$    | $4.85 \times 10^1$    | $5.79 \times 10^1$    |
| $R_{\nu min}$            | $2.69 \times 10^5$    | $2.69 \times 10^5$    | $2.69 \times 10^5$    | $2.69 \times 10^5$    |
| $R_{\nu max}$            | $2.10 \times 10^8$    | $2.50 \times 10^8$    | $2.99 \times 10^8$    | $3.57 \times 10^8$    |
| $Re_0$                   | $1.33 \times 10^4$    | $1.33 \times 10^4$    | $1.33 \times 10^4$    | $1.33 \times 10^4$    |

Table 1: Range of control parameters and dimensionless numbers investigated to test the theory developed in section 3.1.

diffusive regime whose timescale is  $\tau_{2D} = (\rho/(\sigma B_0^2))(h/d_0)^2$  or the propagative regime whose timescale is  $\tau_A = h/V_A$ . As an example, at the highest magnetic field of  $B_0 = 10T$ ,  $\tau_{2D} \approx 5 \times 10^{-4}s$  and  $\tau_A \approx 10^{-3}s$ .

#### 4.4. Experimental procedure

FLOWCUBE offers four dimensional control parameters: the injection scale  $\tilde{d}_0$ , the RMS value of the electric current injected per electrode  $I_0$ , the magnitude of the magnetic field  $B_0$  and the angular frequency of the injected current  $\omega$ . In this study, only the last three parameters were varied so as to independently control non-dimensional parameters  $Re_0$ ,  $Ha$  and  $R_\eta$  ( $Pm = R_\eta/R_\nu = 1.6 \times 10^{-6}$  being set by fluid properties).  $Re_0 = I_0/[2\pi\nu(\sigma\rho\nu)^{1/2}]$  is the Reynolds number based on the forcing current intensity, as defined in Klein & Poth  rat (2010). While variations of  $Ha$  and  $R_\eta$ , all summarised in table 1, enable us to test the linear theory in section 3.1,  $I_0$  and so  $Re_0$  were varied for the specific purpose of assessing the linearity of the wave forcing, and thereby the limits of the linear theory.

Measurements are performed at a constant magnetic field  $B_0$ , *i.e.* at constant  $Ha$ . Starting from a flow at rest, the electric potentials are first recorded during 30s. Then the AC power supply is switched on at a set current angular frequency  $\omega$  and at a RMS value per electrode of the current  $I_0$ . Then, electric potentials are recorded for 30s, to ensure a relative convergence error on  $\phi$  lower than  $10^{-2}$  for all cases. The current supply is then switched off. The last three steps are repeated for different forcing frequencies to span values of  $R_\eta$  and the whole procedure is repeated for different values of the magnetic field in order to span different values of  $Ha$ .

## 5. Experimental results and 4-electrode theoretical model

### 5.1. Methodology for the comparison between theory and experiment

To enable direct comparison between experimental data and the prediction of the low- $Rm$  model, the latter is extended to the case of a 4-electrode configuration representing the experimental current injection pattern. Since the model is linear, this is done by translating the solution for one forcing electrode to the location of each of the four forcing electrodes and superimposing the four solutions so obtained, weighing them by the sign of the current they carry. The solution is then expressed in a common Cartesian frame whose origin is at the centre of the top left electrode of the injection pattern on figure 10. In this frame, we use

two attenuation coefficients and phase shifts defined in a similar way as in §3.2:  $\alpha_x$  and  $\varphi_x$  are based on  $\nabla\phi \cdot e_x$  while  $\alpha$  and  $\varphi$  are based on  $\|\nabla\phi\|$ . Gradients are evaluated by second order central finite differences using signals from adjacent probes, so  $\alpha_x$  and  $\varphi_x$  require the signals of two probes while  $\alpha$  and  $\varphi$  require four.

### 5.2. Oscillating diffusive regime versus propagative regime

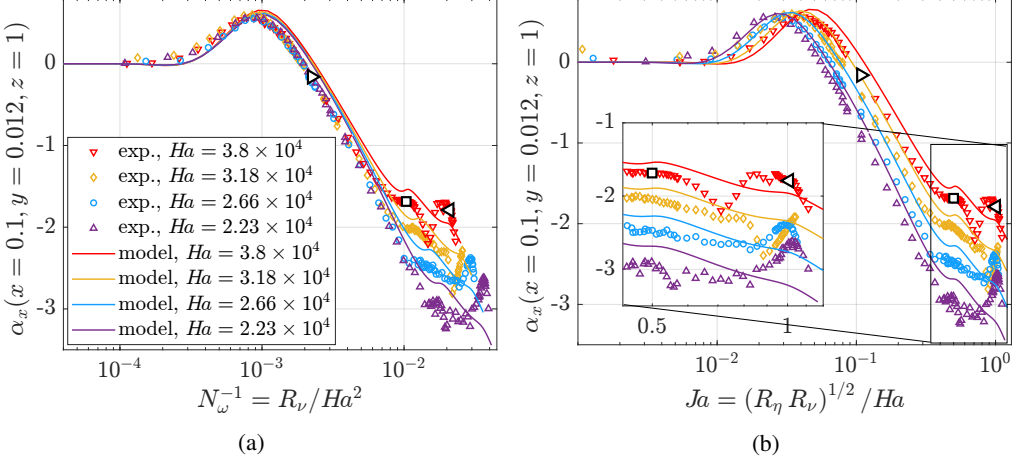


Figure 11:  $\alpha_x$  vs.  $N_\omega^{-1}$  (a) and  $Ja$  (b) for  $Ha = \{1.9 \times 10^4, 2.66 \times 10^4, 3.18 \times 10^4, 3.8 \times 10^4\}$  and  $(x, y, z) = (0.1, 0.012, 1)$ . Solid lines and markers represent the propagative low- $Rn$  model and measurements respectively. White markers ( $\triangleright$ ,  $\square$ ,  $\triangleleft$ ) highlight the cases at  $Ja = 0.1, 0.5$  and  $1$  respectively, all at  $Ha = 3.8 \times 10^4$ , studied in more detail on figures 13, 14 and 15.

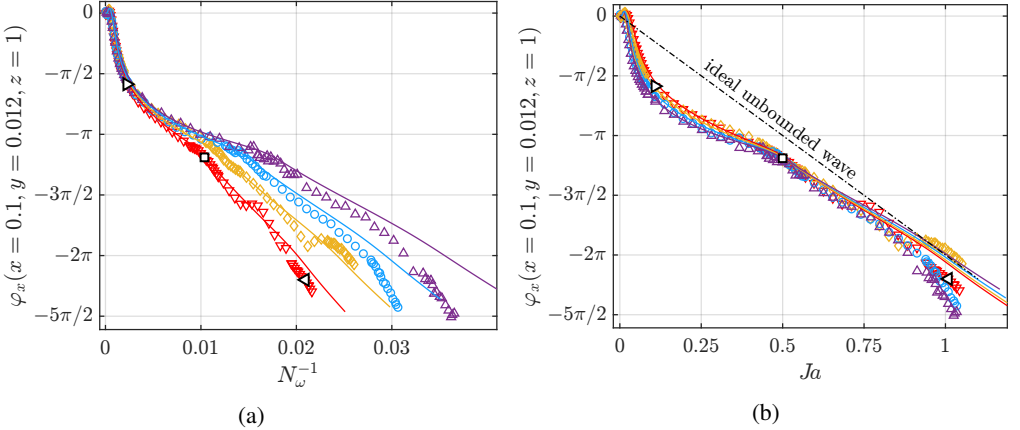


Figure 12:  $\varphi_x$  against  $N_\omega^{-1}$  (a) and  $Ja$  (b) for  $Ha = \{1.9 \times 10^4, 2.66 \times 10^4, 3.18 \times 10^4, 3.8 \times 10^4\}$  and at  $(x, y, z) = (0.1, 0.012, 1)$ . Solid lines and markers represent the propagative low- $Rn$  model and measurements respectively. The dash-dotted line ( $-\cdot-\cdot-$ )  $\varphi_x$  is for an ideal unbounded wave. White markers ( $\triangleright$ ,  $\square$ ,  $\triangleleft$ ) highlight the cases at  $Ja = 0.1, 0.5$  and  $1$  respectively, all at  $Ha = 3.8 \times 10^4$ , studied in more detail on figures 13, 14 and 15.

To track the existence of the diffusive and propagative flow regimes identified in § 3.4,

we first analyse how these quantities vary with the screen parameter  $R_v$ : figures 11 and 12 show  $\alpha_x$  ( $x = 0.1, y = 0.012, z = 1$ ) and  $\varphi_x$  ( $x = 0.1, y = 0.012, z = 1$ ) from both theory and experiments, plotted against  $Ja$  and  $N_\omega^{-1}$ . The variations of both  $\alpha_x$  and  $\varphi_x$  are very similar to those observed for the single-electrode model in § 3. The attenuation coefficient exhibits a plateau in the limit  $N_\omega \rightarrow 0$ , a maximum around  $N_\omega^{-1} = 1 \times 10^{-3}$ , followed by a sharp decay at higher values, with a second peak in the higher frequencies. Similarly, the phase shift  $\varphi_x$  displays two distinct sequences of monotonic decay at low and high screen parameter  $R_v$ , that are qualitatively very similar to those observed for a single electrode. The collapse of both experimental and theoretical data into a single curve for  $(N_\omega)^{-1} \lesssim 5 \times 10^{-3}$  on figures 11a and 12a confirms that the variations of  $\alpha_x$  within this range reflect the spatial attenuation of diffusive oscillations. Similarly, the alignment of resonant peaks at  $Ja = 0.5$  and 1 on figure 11b is a clear signature of resonant waves characteristic of the propagative regime. This point is one of the main results of this work as it shows that intense MHD waves akin to Alfvén waves can be electrically driven at low-Magnetic Reynolds number.

The agreement between theory and experiment is generally excellent, but two distinct types of discrepancies deserve further comments: First, an offset separates the collapsed theoretical from the collapsed experimental values of  $\alpha_x$  (figure 11) resulting in a  $\approx 15\%$  difference in the value of the peak in the diffusive regime and  $\approx 15\%$  in its position. For the propagative peaks, these discrepancies are respectively of  $\approx 10\%$  and  $\approx 3\%$ . However, the experimental data still shows excellent collapse in the diffusive regime and the propagative peak are all well aligned to  $Ja = 0.5$  and 1. Further calculations not reported here show that the actual value of  $\alpha_x$  is quite sensitive to the choice of distribution of injected current across the electrode  $j_w(\mathbf{r})$ . While our simplified model of a Gaussian distribution (3.1) is numerically convenient and roughly reflects the localisation of the injected current at an electrode, it is very different from the complex distribution of current that occurs in the experiment as a result of the interaction between the liquid phase and the solid conductor that forms the electrode (Herreman *et al.* 2019). Hence, this offset can be attributed to our simplified model of the current distribution and we argue that this minor difference does not detract from the excellent agreement between the physical mechanisms taking place in FLOWCUBE and those captured by the model.

The second discrepancy takes place in the high  $R_v$  limit, within the propagative regime: for  $Ja > 0.85$ , both the attenuation and phase shift depart significantly in value and in behaviour from the model. The excellent agreement between theory and model elsewhere suggests that the model misses a physical mechanism in this regime. Since waves propagate more freely in this regime, they reach higher amplitudes and may thus interact nonlinearly, a process that the linear model cannot capture and that requires more specific experimental scrutiny.

### 5.3. Linear and nonlinear flow patterns

Having now identified the diffusive and propagative regimes in the experimental data, we seek to understand the discrepancy between theory and experimental at high values of the Jameson number. To this end, the topology of the flow is investigated using the potential gradients' angle with  $\mathbf{e}_x$  at the Hartmann walls,  $\Theta(z = 0)$  and  $\Theta(z = 1)$ . This quantity has the advantage of ignoring the amplitude of the potential gradient and so reflects solely the topology of the flow. We focus on three different cases: one in the oscillating diffusive regime, one well captured by the model within the propagative regime, and one within the propagative regime but with significant discrepancy between model and experiment. We set  $Ha = 3.8 \times 10^4$  for all three cases corresponding to  $Ja = \{0.1, 0.5, 1\}$  respectively. These cases are highlighted by three different white-filled symbols in figures 11 and 12. Instantaneous experimental and theoretical contours of  $\Theta$  at the top and bottom walls ( $z = 0$  and  $z = 1$ ) are plotted on figure 13 for all three cases.

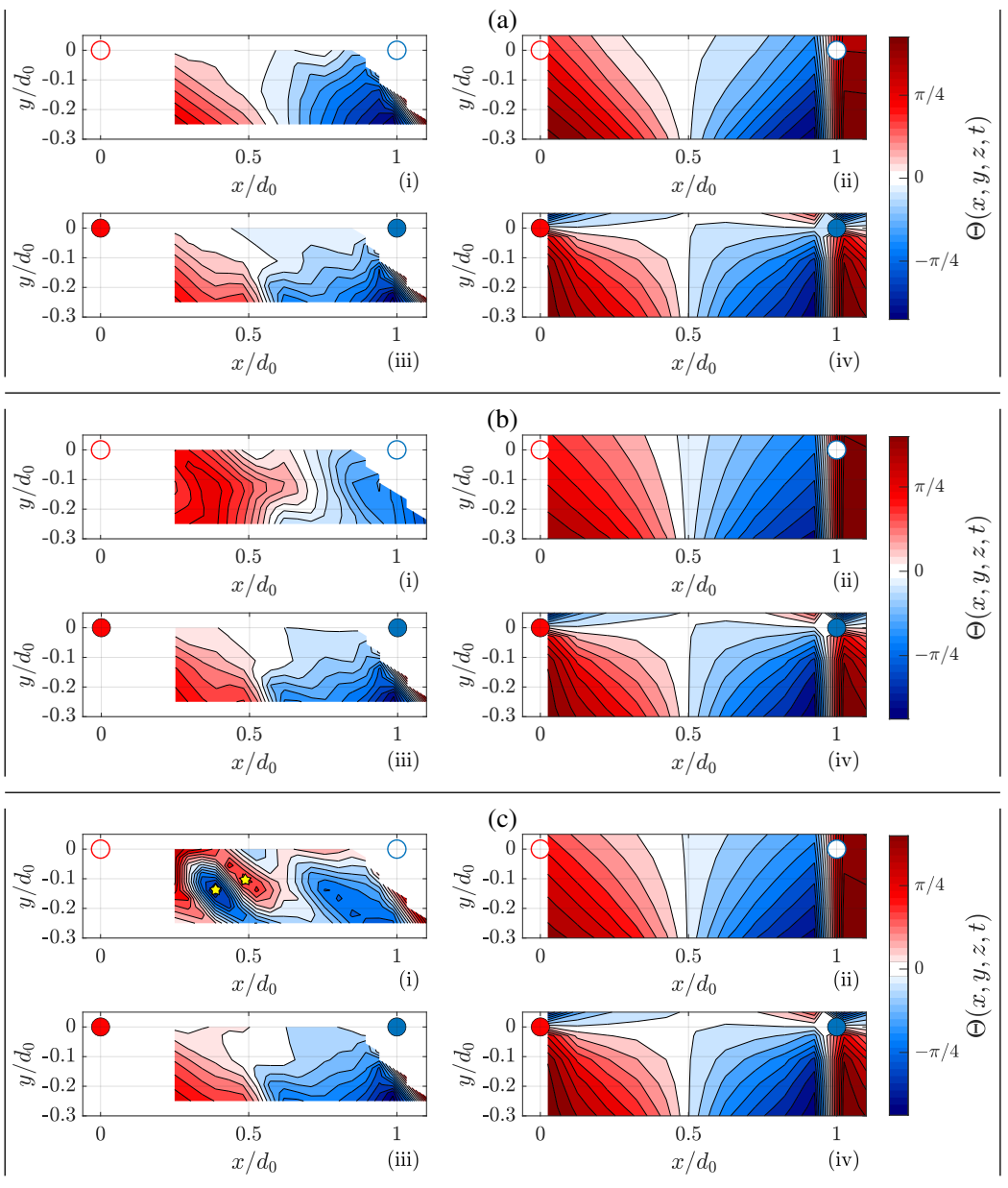


Figure 13: Snapshot contours of  $\Theta$  for  $Ja = 0.1$  (a),  $Ja = 0.5$  (b) and  $Ja = 1$  (c).  $Ha = 3.8 \times 10^4$  for all cases. For each value of  $Ja$ , instantaneous contours of  $\Theta$  are plotted at the top wall (i,ii) and at the bottom wall (iii,iv), from experimental data (i,iii) and from the model (ii,iv). The full coloured circles show the location of two of the four injection electrodes -in phase opposition- while the empty circles show their virtual projection on the top wall. The yellow stars highlights focus points.

For  $Ja = 0.1$  and  $0.5$  (figures 13a and 13b), isolines of  $\Theta$  from experiments are topologically consistent with those from the model. The main difference is that positive iso-values of  $\Theta$

swell slightly toward the positive  $x$ -direction in the experimental data at  $Ja = 0.5$ . While this could be due to nonlinearities, the limited spatial resolution in the experiments and the added uncertainty of comparing instantaneous snapshots make it difficult to reach a definite conclusion regarding the origin of this effect based on these snapshots alone.

For  $Ja = 1$ , the experimental contours of  $\Theta$  are consistent with theory at the bottom wall  $z = 0$ . At the top wall  $z = 1$ , by contrast, two focus points and at least one saddle appear respectively at  $(x, y) = (0.38, -0.14)$  and  $(x, y) = (0.48, -0.11)$  (figure 13c). Further critical points must exist on the top wall to satisfy the topological constraints on their numbers (Hunt *et al.* 1978) but these fall outside of the spatial visualisation window available to us. Because of these, the topology found in the experimental data differs fundamentally from that predicted by the model. This new topological structure is not compatible with the linear prediction, and implies an underpinning nonlinear mechanism. Furthermore, the two focus points are located in the region of the isoline swelling observed for the case  $Ja = 0.5$ , suggesting that the topological change may ensue from small nonlinear deviations to the linear prediction at lower values of  $Ja$ . This also suggests that nonlinearities are favoured at higher values of  $Ja$  and especially near the resonance  $Ja = 1$ , *i.e.* further into the propagative regime, and where the amplitude of the waves is greatest: these conditions are most favourable to the occurrence of nonlinearities and the resonance points to a  $Ja$  nonlinear self-interaction of the wave. Whether an instability mechanism is involved is an open question: instabilities of forced electro-mechanical oscillations were indeed observed, but at  $Ha < 10$ , *i.e.* outside of the propagative regime of relevance here (Thomas *et al.* 2010). In any case, this change in topology corresponds to the discrepancy observed on §5.2 for  $Ja > 0.85$  and so confirms that these discrepancies reflect a nonlinear regime of Alfvén waves, not accounted for in the model.

#### 5.4. Influence of horizontal gradients on the diffusion of oscillations and wave propagation

A key result of the theoretical study in §3.4 was that both the diffusion of oscillations and wave propagation are influenced by the transversal gradients of electric potential. We shall now track and quantify this effect experimentally. The measurements in FLOWCUBE deliver attenuation and phase shifts between the Hartmann walls ( $z = 0$  and  $z = 1$ ) only. Hence, we plot the experimental and theoretical contours of these quantities,  $\alpha(x, y, z = 1)$  and  $\varphi_x(x, y, z = 1)$ , on figures 14 and 15 respectively, again focusing on the case displaying the most prominent wave propagation at high  $Ja$ , *i.e.*  $Ha = 3.8 \times 10^4$  and for  $Ja \in \{0.1, 0.5, 1\}$ .

Experimental contours of  $\alpha$  and  $\varphi_x$  exhibit topologically equivalent patterns to their theoretical counterparts except for  $Ja = 1$  (within the same limitations on the spatial resolution in the experiment and the error incurred by comparing snapshot as in the previous section). The gradients of these quantities visibly decrease with the distance to the neighbouring electrode in all cases but the experimental one at  $Ja = 1$  too. The value of  $\alpha$  itself (figure 14) increases with the transversal distance from each electrode, both in the oscillating diffusive regime (figure 14a-b) and in the linear propagative regime (figure 14c-f) in both theory and experiment. Experimental contours of  $\varphi_x$  are consistent with the model for  $Ja = 0.1$  and  $0.5$  (figure 15). In both cases, the magnitude of  $\varphi_x$  increases with the distance to the neighbouring electrode. These observations concur to show that the high transversal gradients in the vicinity of the electrodes increase the attenuation of the oscillations but accelerate their diffusion and their propagation along  $\mathbf{e}_z$ .

For  $Ja = 1$ , the experimental contours of both  $\alpha$  and  $\varphi_x$  deviate from the model. This case, highlighted by marker ( $\triangleleft$ ) on figures 11 and 12, corresponds to the regime where nonlinear wave interactions incur a change in the flow topology at the top wall (figure 13c), a phenomenon that the linear theory cannot capture. In the experimental data, the locus of the emerging nonlinear pattern coincides with a locally enhanced phase shift compared to



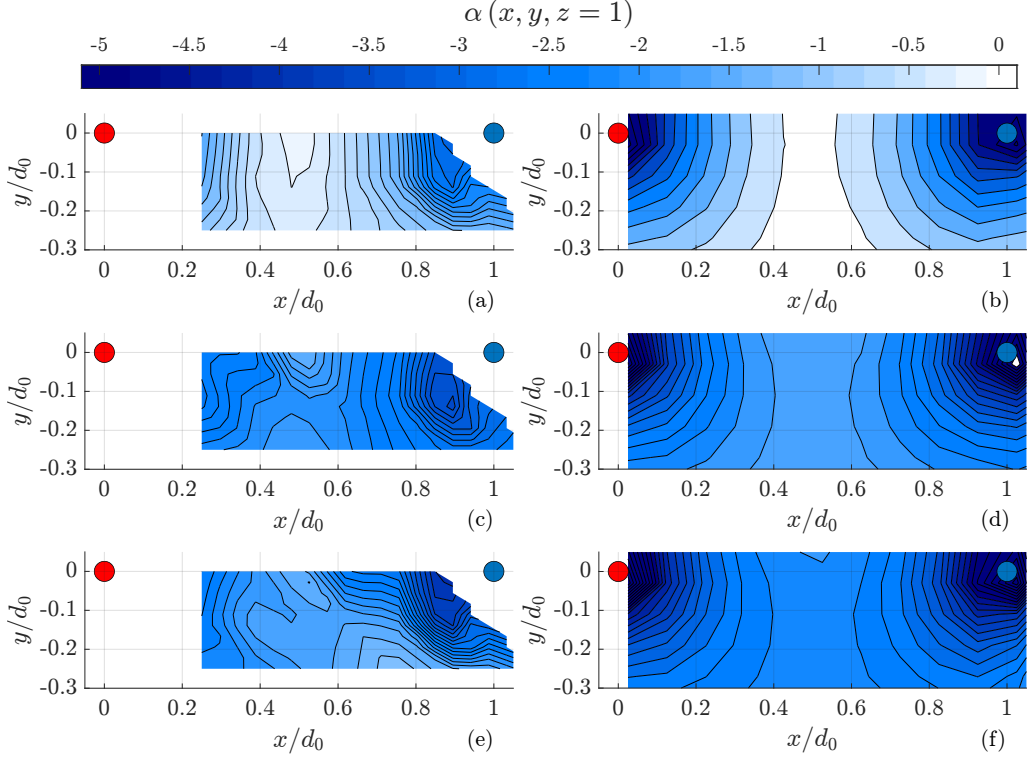


Figure 14: Snapshot contours of  $\alpha$  for  $Ja = 0.1$  (a,b),  $Ja = 0.5$  (c,d) and  $Ja = 1$  (e,f).  $Ha = 3.8 \times 10^4$  for all cases. For each value of  $Ja$ , contours of  $\Theta$  are plotted from experimental data (a,c,e) and from the model (b,d,f). The coloured circles show the location of two electrodes in phase opposition out of the four injection electrodes.

the model, indicating that the nonlinear pattern travels along  $\mathbf{e}_z$  at a different velocity from the fundamental mode driven by the forcing.

To further quantify the dependence of the attenuation and phase shift on the horizontal gradients of electric potential, we take advantage of the near-monotonic dependence of these gradients on the transversal distance to the nearest electrode in the  $(x, y)$  plane, which we denote  $r^*$ . Based on this, the lengthscale of transversal gradients can be approximated by  $r^*$ . We focus on the linear propagative regime where experiments and theory agree well *e.g.*  $Ja = 0.5$ . Figures 16 and 17 respectively show the variations of  $\alpha$  and  $|\varphi_x|$  with  $r^*$  from the experiment and the model. Since these fields are not axisymmetric about either of the electrodes, these variations also depend on the azimuthal angle with respect to the closest electrode, especially for points that are nearly equidistant from two electrodes. The theoretical range of variation of  $\alpha$  and  $\varphi_x$  spanned in this way is represented on the figures by a red zone. The experimental data shows a greater spread attributed to the local measurement error, of around 4%, and to the offset in damping rate incurred by our simplified model of the current distribution at the electrode (see § 5.2). Nevertheless, the experimental values of  $\alpha$  are consistent with the model. In both cases,  $\alpha$  increases with  $r^*$ . These variations do not appear to follow a simple scaling law. Indeed, the values of  $r^*$  fall in an intermediate range between the regime of low transversal gradient investigated by Jameson (1964) and a regime of much higher transversal gradient where waves are highly damped. In the high damping regime, horizontal gradients are sufficiently strong to incur magnetic dissipation comparable

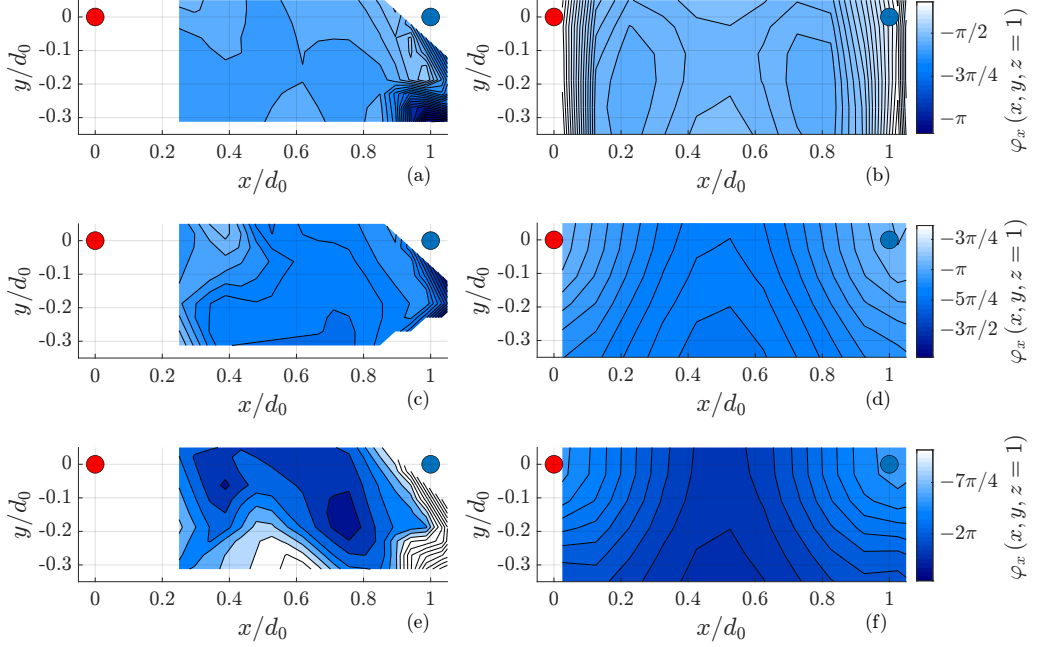


Figure 15: Snapshot contours of  $\varphi_x$  for  $Ja = 0.1$  (a,b),  $Ja = 0.5$  (c,d) and  $Ja = 1$  (e,f).  $Ha = 3.8 \times 10^4$  for all cases. For each value of  $Ja$ , the contours of  $\Theta$  are plotted from experimental data (a,c,e) and from the model (b,d,f). The coloured circles show the location of two electrodes in phase opposition out of the four injection electrodes.

to the axial ones, and so considerably increase the damping of oscillations along  $e_z$ . This phenomenon takes place in the deep blue area very close to the electrode in figure 5(c). The vertical contours of  $\alpha$  obtained from the single electrode theory show that this region extends over the entire height of the vessel. In the QSMHD limit, this region becomes the classical viscous vortex core of inertialess thickness  $\sim Ha^{1/2}$  studied in detail by Sommeria (1988).

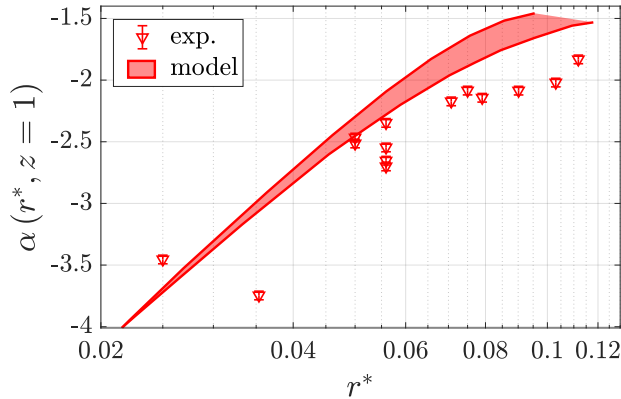


Figure 16:  $\alpha$  vs.  $r^*$  for  $Ja = 0.5$  and  $Ha = 3.8 \times 10^4$ .  $r^*$  is the distance in the  $(x, y)$  plane between a given measurement location and the nearest injection electrode. The solid line and markers correspond to the propagative low- $Rn$  model and measurements respectively. The error bars show the local measurements errors for  $\alpha$ , of 4%.

Similarly, the magnitude of the phase shift  $\varphi_x$  increases with  $r^*$  in both experiment and

model, without following any obvious scaling law (figure 17). It should also be noticed that the scattering from experiments is more important for  $|\varphi_x|$  than for  $\alpha$ . The scattering can be attributed to several factors: first, using a single component of the potential gradient  $\varphi_x$  incurs errors when the gradient is close to normal to that direction. Second, the most scattered points fall mostly in the region where discrepancies in flow topologies were observed between theory and experiment. This suggests that the scattering may arise out of nonlinear effects.

The variations of  $\alpha$  and  $\phi$  quantify the previous observation that stronger transversal gradients damp the waves whilst accelerating their propagation. Additionally, they show that the dissipative waves observed in FLOWCUBE sit at an intermediate regime of dissipation. As such, less dissipative waves may be obtained in a different geometry minimising transversal gradient. Jameson (1964) had indeed identified this effect and used it to maximise the intensity of the waves he could observe within the physical limitations of his experiment and despite the relatively low magnetic field available to him. The quality of the results he obtained in this manner, compared to other experiments available in these times (Lundquist 1949; Bostick & Levine 1952; Lehnert 1954; Allen *et al.* 1959) is indeed a tribute to his deep understanding of the subtleties of these waves.

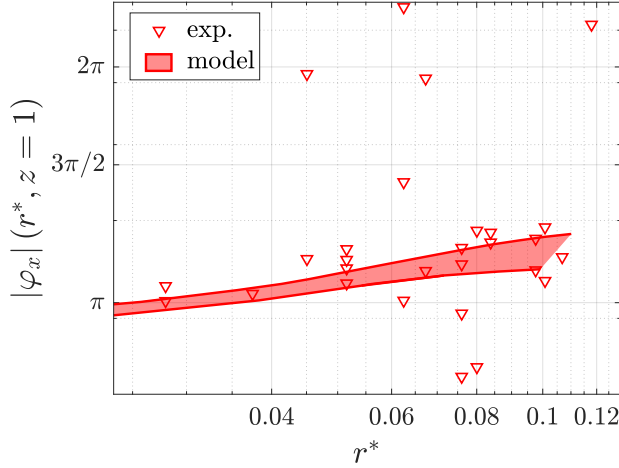


Figure 17:  $\varphi_x$  against  $r^*$  for  $Ja = 0.5$  and  $Ha = 3.8 \times 10^4$ .  $r^*$  is the distance in the (x,y) plane between a given measurement location and the nearest injection electrode. The solid line and the light red coloured area exhibit model's prediction while markers show measurements.

### 5.5. Linearity and nonlinearity of the experimental waves

The discrepancies between model and experiment at high Jameson numbers ( $Ja \gtrsim 0.85$ ) in §5.2 revealed significant nonlinearities in this regime. Smaller discrepancies between theoretical and experimental contours of the potential gradient angle may further suggest that these nonlinearities develop at lower Jameson numbers ( $Ja \approx 0.5$ ). Hence, notwithstanding the otherwise excellent agreement between theory and experiment, the question arises as to which regime of controlled parameters sees nonlinearities affecting either the oscillating diffusive regime or the propagative one. In particular, how much of the experimental data may fall within this regime? To answer these questions, we assess the linearity of electric potential gradients with respect to the forcing intensity. Dimensionally, the forcing intensity is controlled by the total current injected in the flow, and nondimensionally, it is measured by  $Re_0$ . Nonlinearities are assessed using the average intensity of the electric potential gradients,

and their relative nonlinearity is defined as

$$\epsilon_{\text{NL}} = \left| 1 - \frac{\left\langle \left| \widehat{\nabla_x \phi}(Re_0) \right| \right\rangle_{x,y}}{Re_0} \lim_{Re_0 \rightarrow 0} \frac{Re_0}{\left\langle \left| \widehat{\nabla_x \phi}(Re_0) \right| \right\rangle_{x,y}} \right|, \quad (5.1)$$

where  $|\widehat{\nabla_x \phi}|$  refers to the amplitude of the oscillations of  $\partial_x \phi$  while  $\langle \cdot \rangle_{x,y}$  denotes the operator for spatial averaging in the  $(x, y)$  plane. For flows purely within the linear regime,  $\epsilon_{\text{NL}} = 0$ . To assess this quantity, the purely linear solution in the limit  $Re_0 \rightarrow 0$  is approximated by the experimental data obtained at the lowest value of  $Re_0$ , *i.e.*  $Re_0 = 3.75 \times 10^3$ . The relative nonlinearity of the potential gradient  $\epsilon_{\text{NL}}$  is plotted at the bottom and top walls for  $Ha = \{3.18 \times 10^4, 3.8 \times 10^4\}$  and  $Ja = \{0.1, 0.5, 1\}$  (figure 18). In all cases,  $\epsilon_{\text{NL}}$  smoothly increases with  $Re_0$ . Thus, nonlinearities are always present, albeit in vanishingly small amount in the limit  $Re_0 \rightarrow 0$ . This concurs to the observation of small discrepancies in the contours of the angle of electric potential gradients  $\Theta$  (figure 13b-c), even in regimes where theoretical values of both the attenuation coefficient and phase shift agree well with the experimental ones.

At the bottom wall,  $\epsilon_{\text{NL}}$  remains below 6% for all cases (figure 18b). A saturation in the variations of  $\epsilon_{\text{NL}}(Re_0)$  however takes places around  $Re_0 \simeq 2 \times 10^4$ , and only in the propagative regime  $Ja \geq 0.5$  (for  $\{Ha = 3.8 \times 10^4, Ja = 0.5\}$  and  $\{Ha = 3.8 \times 10^4, Ja = 1\}$ ) (figure 18b). This is indicative of a change in nonlinear dynamics with a possible dominance of nonlinear wave interaction. By contrast, flows within the diffusive regime remain essentially linear for the entire range of forcing spanned within the experiment. Data at the top wall (figure 18a) reveal the same phenomenology but with significantly greater nonlinearity, up to  $\simeq 40\%$ . This also concurs with the observations of the contours of  $\Theta$ , where the discrepancy between theory and experiment was found greater near the top wall. This further supports the idea that nonlinearities arise from nonlinear wave interaction. Indeed, these interactions are impeded near the bottom wall where patterns of injected current are imposed. However, they grow as they propagate away from the forcing region, and so are more likely observed near the top wall.

Except for the present section, all experimental data shown in this work were obtained for  $Re_0 = 1.33 \times 10^4$  (highlighted with dashed lines on figure 18a and 18b). For this forcing intensity,  $\epsilon_{\text{NL}}$  remains lower than  $\simeq 12\%$  for all cases but  $Ha = 3.8 \times 10^4, Ja = 1$ . Hence, it can be concluded that the phenomenology discussed throughout this work is linear in all regimes where experiment and theory agree. Nevertheless, the data at higher  $Re_0$  discussed in this section clearly shows that nonlinear regimes are easily reached within FLOWCUBE's operational range of parameters.

## 6. Conclusion

We studied an electrically driven oscillating flow confined between two walls perpendicular to an externally imposed magnetic field, in view of identifying the conditions in which diffusive, propagative and nonlinear processes occur in low- $Rm$  magnetohydrodynamics. The underlying question at stake is whether Alfvén waves observed in astro- and geophysical systems can be studied in detail in laboratory-scale experiments using liquid metals. To address this problem, we developed two linear models, one based on a propagative extension of the usual low- $Rm$  MHD approximation, and one based on the Quasi-Static MHD (QSMHD) approximation. We also adapted the FLOWCUBE experimental device (Klein & Pothérat 2010) to directly track these regimes in a rectangular vessel filled with liquid metal. The propagative low- $Rm$  approximation differs from the usual QSMHD approximation in that the

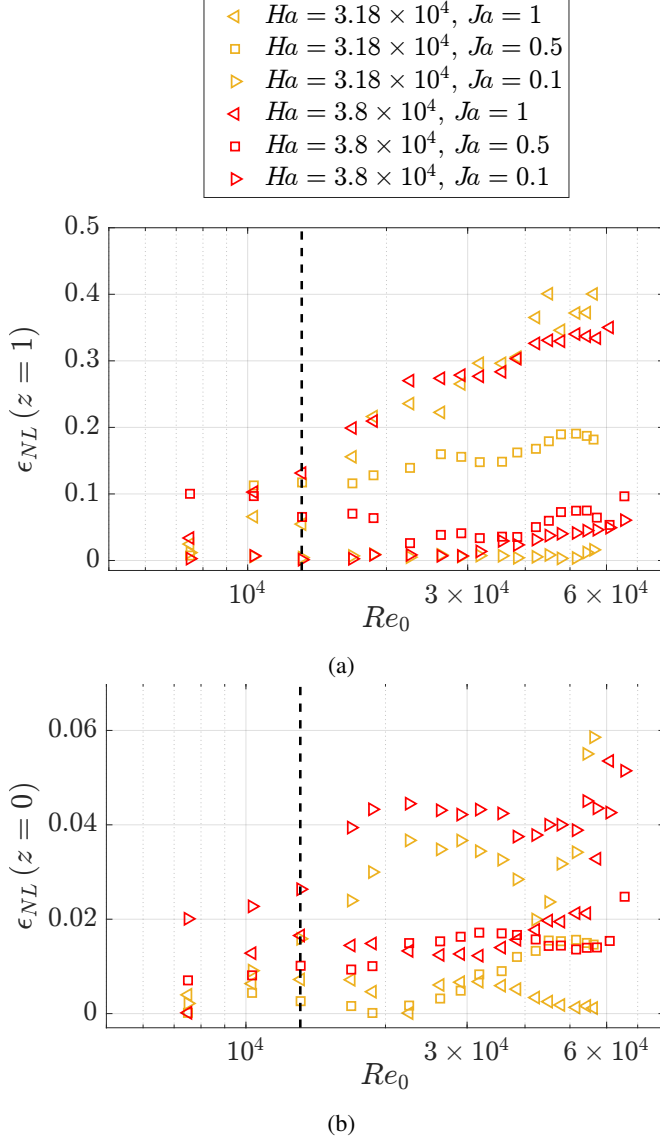


Figure 18: Normalised  $\langle |\widehat{\nabla_x \phi}| \rangle$  against  $Re_0$  at the top wall (a) and the bottom wall (b) for  $Ha = \{3.18 \times 10^4, 3.8 \times 10^4\}$  and  $Ja = \{0.1, 0.5, 1\}$ . For each case of the set  $\{Ha, Ja\}$ ,  $\langle |\widehat{\nabla_x \phi}| \rangle$  is normalised by its value at the lowest experimental  $Re_0$ .

time scale of local oscillations is different from the flow turnover time. In the limit of vanishing Reynolds number. It is therefore governed by three non-dimensional parameters: the usual Hartmann number  $Ha = Bh(\sigma/(\rho\nu))^{1/2}$  and two screen parameters, a viscous one,  $R_\nu = \omega h^2/(2\pi\nu)$  and a resistive one  $R_\eta = \omega h^2/(2\pi\eta)$ . The linearised QSMHD approximation is recovered in the limit  $R_\eta \rightarrow 0$ , keeping  $R_\nu$  finite.

Combining theory and experiments enabled us to identify and characterise three different regimes of forced oscillations. The first regime falls within the QSMHD approximation. It is captured by both linear models and experiments and occurs at low screen parameters  $R_\nu$

or  $R_\eta$ . In this regime, the Lorentz force acts exclusively so as to diffuse momentum along magnetic field lines. In the limit  $R_\eta \rightarrow 0$ , this diffusion process drives flows towards a quasi-two dimensional state (Sommeria & Moreau 1982). Hence, we called this regime *oscillating diffusive*, and found that it is characterised by an oscillating parameter  $N_\omega = 2\pi\sigma B_0^2/\rho\omega$  built out of the ratio of the oscillation timescale  $2\pi/\omega$  to the two-dimensionalisation timescale at the scale of the box, associated to the Lorentz force,  $\tau_{2D} = \rho/(\sigma B_0^2)$ , first introduced by Sommeria & Moreau (1982). The second regime occurs at higher values of  $R_\eta$ . It is captured by experiments in excellent agreement with the linear propagative low- $Rm$  model, but not by the QSMHD model. This linear *propagative* regime is dominated by the propagation of Alfvén waves. Their resonance across the channel occurs at values of  $R_\eta$  such that the ratio between the propagation time of Alfvén waves across the channel and the oscillation period is either 1/4, 1/2, 3/4 or 1. The second regime is characterised by values of this ratio, which we named the *Jameson number*  $Ja = \omega h/(2\pi V_A)$  below  $\simeq 0.85$ . The existence of this regime is one of the chief results of this study as it establishes that MHD waves akin the Alfvén waves but different from ideal AW can propagate at low  $Rm$ . The third regime occurs at the highest values of  $R_\eta$ , corresponding to  $Ja \gtrsim 0.85$  and therefore remains propagative in nature. It emerges where wave amplitudes are too high for the linear model to remain valid (most noticeably near the resonance  $Ja = 1$ ). Indeed, experimental data departs from the linear model, and displays a clear nonlinear behaviour. Hence we name this regime the *nonlinear propagative regime*.

The particular type of AW we found in the propagative regime, further exhibit unique propagation properties so far unobserved at low- $Rm$ . In the linear propagative regime, both the model and the experimental data display a dependence of the phase velocity on  $R_\eta$ , so unlike ideal AW, these waves are dispersive. Furthermore, the configuration involves a spatially inhomogeneous forcing in the planes perpendicular to the magnetic field with electric potential gradients decaying away from the points of current injection. This provided us an opportunity to analyse how such inhomogeneity affects wave propagation. Indeed, both model and experiment clearly show that the propagation of these dispersive Alfvén waves depends on the transversal gradients: they are both locally accelerated and more strongly damped in stronger gradients. Such variations of propagation velocity, never observed before at low- $Rm$ , is sometimes referred to as *phase mixing*. It locally increases the viscous and resistive wave dissipation responsible for a heating process that may play a role in the Sun's corona heating (Heyvaerts & Priest 1983; McLaughlin *et al.* 2011; Prokopyshyn *et al.* 2019).

Outside the linear propagative regime, nonlinearities manifest themselves in several ways: First, contour maps of electric potential reveal a change in the flow topology, noticeable near the top Hartmann wall, *i.e.* further away from the forcing point. This, together with the occurrence near a resonance of these nonlinearities, supports the hypothesis of nonlinear self interaction of Alfvén waves. Additionally, varying the forcing intensity expressed by Reynolds number  $Re_0$  for different values of  $Ja$  values shows stronger departure from the linear model at higher amplitudes, another signature of nonlinearity. The discrepancy from linearity was further found to increase continuously from very small  $Re_0$  and so suggests that nonlinearities are always present, rather than ignited near a bifurcation as the forcing amplitude increases. The presence of nonlinearities driven by wave self-interaction is another major result and so answers one of the key questions that motivated this work: nonlinear energy transfers can be reproduced in liquid metal experiments. This paves the way for the study of a second mechanism directly relevant to processes expected to take place in astrophysical systems, especially the solar corona (Davila 1987; Holst *et al.* 2014).

The three regimes found in this work show that all three key ingredients of astro- and geophysical AW can be reproduced in a small-scale experiment: diffusion, propagation and nonlinearity. Additionally, we have been able to characterise the inhomogeneous properties



of dispersive AW, another key feature of the complex dynamics of AW in these systems. These results open a new spectrum of opportunities to model such practically inaccessible objects as planetary interiors or the solar corona in the relative comfort of a small-scale laboratory, using liquid metals. We are certainly a long way from bringing the physics of the sun into a box filled with liquid metal. But we are almost an equally long way from having exhausted the possibilities offered by the increasingly high intensity of magnetic fields available to liquid metal experiments, and the range of possibilities offered by electrically driven AW: varying the forcing intensity, the forcing geometry, the shape size of the box offer as many opportunities to seek more intense nonlinearities, different types of inhomogeneities and of nonlinear effects. Each of these may hold the key to some aspects of how AW behave in the Sun or in planetary interiors.

## REFERENCES

- ALBOUSSIERE, THIERRY, CARDIN, PHILIPPE, DEBRAY, FRANÇOIS, LA RIZZA, PATRICK, MASSON, JEAN-PAUL, PLUNIAN, FRANCK, RIBEIRO, ADOLFO & SCHMITT, DENYS 2011 Experimental evidence of Alfvén wave propagation in a Gallium alloy. *Physics of Fluids* **23** (9), 096601, number: 9 Publisher: American Institute of Physics.
- ALFVÉN, H. 1942 Existence of Electromagnetic-Hydrodynamic Waves. *Nature* **150** (3805), 405–406, number: 3805.
- ALLEN, T. K., BAKER, WILLIAM R., PYLE, ROBERT V. & WILCOX, JOHN M. 1959 Experimental generation of plasma Alfvén waves. *Phys. Rev. Lett.* **2**, 383–384.
- ANDREEV, OLEG, KOLESNIKOV, YURI & THESS, ANDRÉ 2013 Visualization of the Ludford column. *Journal of Fluid Mechanics* **721**, 438–453, publisher: Cambridge University Press.
- AUJOGUE, KÉLIG, POTHÉRAT, ALBAN, BATES, IAN, DEBRAY, FRANÇOIS & SREENIVASAN, BINOD 2016 Little Earth Experiment: An instrument to model planetary cores. *Review of Scientific Instruments* **87** (8), 084502.
- BAKER, NATHANIEL T., POTHÉRAT, ALBAN & DAVOUST, LAURENT 2015 Dimensionality, secondary flows and helicity in low-rm MHD vortices. *J. Fluid Mech.* **779**, 325–350.
- BAKER, NATHANIEL T., POTHÉRAT, ALBAN, DAVOUST, LAURENT & DEBRAY, FRANÇOIS 2018 Inverse and direct energy cascades in three-dimensional magnetohydrodynamic turbulence at low magnetic Reynolds number. *Phys. Rev. Lett.* **120** (22), 224502, number: 22 Publisher: American Physical Society.
- BAKER, NATHANIEL T., POTHÉRAT, ALBAN, DAVOUST, LAURENT, DEBRAY, FRANÇOIS & KLEIN, RICO 2017 Controlling the dimensionality of low-Rm MHD turbulence experimentally. *Exp. Fluids* **58** (7), 79.
- BATCHELOR, G. K. 1967 *An Introduction to Fluid Dynamics*. Cambridge Mathematical Library 683. Cambridge: Cambridge University Press.
- BOSTICK, WINSTON H. & LEVINE, MORTON A. 1952 Experimental demonstration in the laboratory of the existence of magneto-hydrodynamic waves in ionized helium. *Phys. Rev.* **87**, 671–671.
- BRAGINSKY, S.I. 1970 Torsional magnetohydrodynamic vibrations in the Earth's core and variations in day length. *Geomagn. Aeron.* **10** (1), 3–12.
- BRITO, D., NATAF, H. C., CARDIN, P., AUBERT, J. & P., MASSON J. 2001 Ultrasonic doppler velocimetry in liquid gallium. *Exp. Fluids* **31** (6), 653–663.
- CARTER, T. A., BRUGMAN, B., PRIBYL, P. & LYBARGER, W. 2006 Laboratory observation of a nonlinear interaction between shear alfvén waves. *Phys. Rev. Lett.* **96**, 155001.
- CATTELL, CA 1996 Experimental evaluation of the Lundquist number for the Earth's magnetopause and magnetotail. *Journal of Geophysical Research: Space Physics* **101** (A12), 27309–27316.
- DAVIDSON, P. A. 2001 *An Introduction to Magnetohydrodynamics*. Cambridge University Press.
- DAVILA, JOSEPH M. 1987 Heating of the Solar Corona by the Resonant Absorption of Alfvén Waves. *ApJ* **317**, 514.
- DORFMAN, S. & CARTER, T. A. 2013 Nonlinear excitation of acoustic modes by large-amplitude Alfvén waves in a laboratory plasma. *Phys. Rev. Lett.* **110**, 195001.
- DORFMAN, S. & CARTER, T. A. 2016 Observation of an Alfvén wave parametric instability in a laboratory plasma. *Phys. Rev. Lett.* **116**, 195002.
- DYMKOU, V. & POTHÉRAT, A. 2009 Spectral methods based on the least dissipative modes for wall bounded MHD flows. *Theoretical and Computational Fluid Dynamics* **23** (6), 535–555.

- ENNAYAR, H, KARCHER, C & BOECK, T. 2021 Numerical simulation of Stokes' second problem affected by magnetic field. In *Proceedings of the 10th international conference Electromagnetic Processing of Materials Riga, Latvia, June 14-16*.
- FINLAY, CHRISTOPHER 2007 *Alfvén Waves*, pp. 3–6. Dordrecht: Springer Netherlands.
- FINLAY, CHRISTOPHER C. 2008 Course 8 waves in the presence of magnetic fields, rotation and convection. *Les Houches Summer School Proceedings* **88**, 403 – 450, cited by: 27.
- FRANK, M., BARLEON, L. & MÜLLER, U. 2001 Visual analysis of two-dimensional magnetohydrodynamics. *Phys. Fluids* **13** (8), 2287–2295.
- FRANKE, SVEN, BÜTTNER, LARS, CZARSKIE, JÜRGEN, RÄBIGER, DIRK & ECKERT, SVEN 2010 Ultrasound doppler system for two-dimensional flow mapping in liquid metals. *Flow Measurement and Instrumentation* **21** (3), 402–409.
- GEKELMAN, WALTER, VINCENA, STEPHEN, LENEMAN, DAVID & MAGGS, JAMES 1997 Laboratory experiments on shear Alfvén waves and their relationship to space plasmas. *Journal of Geophysical Research: Space Physics* **102** (A4), 7225–7236.
- GILLET, NICOLAS, GERICK, FELIX, JAULT, DOMINIQUE, SCHWAIGER, TOBIAS, AUBERT, JULIEN & ISTAS, MATHIEU 2022 Satellite magnetic data reveal interannual waves in Earth's core. *Proceedings of the National Academy of Sciences* **119** (13), e2115258119.
- GILLET, N., JAULT, D. & CANET, E. ET AL. 2010 Fast torsional waves and strong magnetic field within the Earth's core. *Nature* **465**, 74–77.
- GRANT, S.D.T., JESS, D.B., ZAQARASHVILI, T.V., BECK, C., SOCCAS-NAVARRO, H., ACHAWANDEN, M. J., KEYS, P. H., CHRISTIAN, D. J., HOUSTON, S. J. & HEWITT, R. L. 2018 Alfvén wave dissipation in the solar chromosphere. *Nature Phys* **14**, 480–483.
- HANASOGE, SHRAVAN, BIRCH, AARON, GIZON, LAURENT & TROMP, JEROEN 2012 Seismic probes of solar interior magnetic structure. *Physical review letters* **109** (10), 101101.
- HERREMAN, W., NORE, C., ZIEBELL RAMOS, P., CAPPANERA, L., GUERMOND, J.-L. & WEBER, N. 2019 Numerical simulation of electrovortex flows in cylindrical fluid layers and liquid metal batteries. *Physical Review Fluids* **4** (11), 113702.
- HEYVAERTS, J & PRIEST, ERIC R 1983 Coronal heating by phase-mixed shear Alfvén waves. *Astronomy and Astrophysics* **117** (2), 220–234.
- HOLST, B. VAN DER, SOKOLOV, I. V., MENG, X., JIN, M., W. B. MANCHESTER, IV, TÓTH, G. & GOMBOSI, T. I. 2014 Alfvén wave solar model (AWSOM): Coronal heating. *The Astrophysical Journal* **782** (2), 81.
- HORI, KUMIKO, JONES, CHRIS A, ANTUÑANO, ARRATE, FLETCHER, LEIGH N & TOBIAS, STEVEN M 2023 Jupiter's cloud-level variability triggered by torsional oscillations in the interior. *Nature Astronomy* **7** (7), 825–835.
- HOWES, G. G. 2015 A dynamical model of plasma turbulence in the solar wind. *Phil. Trans. R. Soc. A*. p. 3732014014520140145.
- HOWES, G. G., DRAKE, D. J., NIELSON, K. D., CARTER, T. A., KLETZING, C. A. & SKIFF, F. 2012 Toward astrophysical turbulence in the laboratory. *Phys. Rev. Lett.* **109**, 255001.
- HOWES, G. G., NIELSON, K. D., DRAKE, D. J., SCHROEDER, J. W. R., SKIFF, F., KLETZING, C. A. & CARTER, T. A. 2013 Alfvén wave collisions, the fundamental building block of plasma turbulence. III. Theory for experimental design. *Physics of Plasmas* **20** (7), 072304.
- HUNT, J. C. R., ABELL, C. J., PETERKA, J. A. & WOO, H. 1978 Kinematical studies of the flows around free or surface-mounted obstacles; applying topology to flow visualization. *J. Fluid Mech.* **86** (1), 179–200.
- IWAI, K., SHINYA, K. & TAKASHI, K. MOREAU, R. 2003 Pressure change accompanying Alfvén waves in a liquid metal. *Magnetohydrodynamics* **39** (3), 245–250.
- JAMESON, ANTONY 1964 A demonstration of Alfvén waves Part 1. Generation of standing waves. *Journal of Fluid Mechanics* **19** (4), 513–527, number: 4.
- JAULT, D. & FINLAY, C.C. 2015 8.09 - waves in the core and mechanical core–mantle interactions. In *Treatise on Geophysics (Second Edition)*, Second edition edn. (ed. Gerald Schubert), pp. 225–244. Oxford: Elsevier.
- JEPHCOTT, DF & STOCKER, PM 1962 Hydromagnetic waves in a cylindrical plasma: an experiment. *Journal of Fluid Mechanics* **13** (4), 587–596.
- KLEIN, R. & POTHÉRAT, A. 2010 Appearance of three dimensionality in wall-bounded MHD flows. *Phys. Rev. Lett.* **104** (3), 034502, number: 3 Publisher: American Physical Society.
- KLEIN, R, POTHÉRAT, A & ALFERENOK, ARTEM 2009 Experiment on a confined electrically driven vortex pair. *Physical review. E* **79**, 016304.

- KLJUKIN, A. & THESS, A. 1998 Direct measurement of the stream-function in a quasi-two-dimensional liquid metal flow. *Experiments in Fluids* **25** (4), 298–304.
- KORNET, KACPER & POTHÉRAT, ALBAN 2015 A method for spectral DNS of low Rm channel flows based on the least dissipative modes. *Journal of Computational Physics* **298**, 266–279.
- LEHNERT, BO 1954 Magneto-Hydrodynamic Waves in Liquid Sodium. *Physical Review* **94** (4), 815–824, number: 4.
- LI, XINYU, BELOBORODOV, ANDREI M. & SIRONI, LORENZO 2021 Fast dissipation of colliding Alfvén waves in a magnetically dominated plasma. *The Astrophysical Journal* **915** (2), 101.
- LUNDQUIST, S. 1949 Experimental Investigations of Magneto-Hydrodynamic Waves. *Physical Review* **76** (12), 1805–1809, number: 12.
- LUO, JIAWEN & JACKSON, ANDREW 2022 Waves in the Earth’s core. i. mildly diffusive torsional oscillations. *Proc. R. Soc. A* p. 4782021098220210982.
- MAJUMDER, DEBARSHI & SREENIVASAN, BINOD 2023 The role of magnetic waves in tangent cylinder convection. *Physics of the Earth and Planetary Interiors* **344**, 107105.
- MCLAUGHLIN, J. A., DE MOORTEL, I. & HOOD, A. W. 2011 Phase mixing of nonlinear visco-resistive Alfvén waves. *Astronomy & Astrophysics* **527**, A149.
- MOFFATT, H. K. 1967 On the suppression of turbulence by a uniform magnetic field. *J. Fluid Mech.* **28**, 571–592.
- MOREAU, R. 1990 *Magnetohydrodynamics*. Kluwer Academic Publisher.
- MOUDJED, B., POTHÉRAT, A. & HOLDSWORTH, M. 2020 PIV mapping of pressure and velocity fields in the plane magnetohydrodynamic Couette flow. *Experiments in Fluids* **61** (12), 255.
- NAKARIAKOV, VALERY M. & KOLOTKOV, DMITRII Y. 2020 Magnetohydrodynamic waves in the solar corona. *Annual Review of Astronomy and Astrophysics* **58**, 441–481.
- NAKARIAKOV, V. M., L., OFMAN., DELUCA, E. E., B., ROBERTS & DAVILA, J. M. 1999 Trace observation of damped coronal loop oscillations: Implications for coronal heating. *Science* **285** (5429), 862–864.
- NORNBERG, MD, JI, H, SCHARTMAN, E, ROACH, A & GOODMAN, J 2010 Observation of magnetocoriolis waves in a liquid metal Taylor-Couette experiment. *Physical review letters* **104** (7), 074501.
- POTHÉRAT, A. & KLEIN, R. 2017 Do magnetic fields enhance turbulence at low magnetic Reynolds number ? *Phys. Rev. Fluids* **2** (6), 063702.
- POTHÉRAT, A. & ALBOUSSIÈRE, T. 2003 Small scales and anisotropy in low- $Rm$  magnetohydrodynamic turbulence. *Physics of Fluids* **15** (10), 3170–3180.
- POTHÉRAT, ALBAN & ALBOUSSIÈRE, THIERRY 2006 Bounds on the attractor dimension for low- $Rm$  wall-bound magnetohydrodynamic turbulence. *Physics of Fluids* **18** (12), 125102.
- POTHÉRAT, ALBAN & DYMOKU, VITALI 2010 Direct numerical simulations of low- $Rm$  MHD turbulence based on the least dissipative modes. *Journal of Fluid Mechanics* **655**, 174–197, publisher: Cambridge University Press.
- POTHÉRAT, ALBAN & KLEIN, RICO 2014 Why, how and when MHD turbulence at low becomes three-dimensional. *Journal of Fluid Mechanics* **761**, 168–205, publisher: Cambridge University Press.
- POTHÉRAT, ALBAN & KORNET, KACPER 2015 The decay of wall-bounded MHD turbulence at low. *Journal of Fluid Mechanics* **783**, 605–636, publisher: Cambridge University Press.
- PROKOPYSZYN, A. P. K., HOOD, A. W. & DE MOORTEL, I. 2019 Phase mixing of nonlinear Alfvén waves. *Astronomy & Astrophysics* **624**, A90.
- ROBERTS, P. H. 1967 *An introduction to magnetohydrodynamics*. New York: American Elsevier Pub. Co., open Library ID: OL14117453M.
- SALEM, CHADI S, HOWES, GG, SUNDKVIST, D, BALE, SD, CHASTON, CC, CHEN, CHK & MOZER, FS 2012 Identification of kinetic alfvén wave turbulence in the solar wind. *The Astrophysical Journal Letters* **745** (1), L9.
- SCHAEFFER, NATHANAËL, JAULT, DOMINIQUE, CARDIN, PHILIPPE & DROUARD, MARIE 2012 On the reflection of Alfvén waves and its implication for Earth’s core modelling. *Geophysical Journal International* **191** (2), 508–516.
- SCHMITT, DENYS, CARDIN, PHILIPPE, LA RIZZA, PATRICK & NATAF, H-C 2013 Magneto-coriolis waves in a spherical Couette flow experiment. *European Journal of Mechanics-B/Fluids* **37**, 10–22.
- SCHWAIGER, T., GILLET, N., JAULT, D., ISTAS, M. & MANDEA, M. 2024 Wave-like motions and torques in Earth’s core as inferred from geomagnetic data: A synthetic study. *Physics of the Earth and Planetary Interiors* **346**, 107104.
- SINGH, KAP & SUBRAMANIAN, PRASAD 2007 An evaluation of possible mechanisms for anomalous resistivity in the solar corona. *Solar Physics* **243**, 163–169.

- SOMMERIA, JOËL 1986 Experimental study of the two-dimensional inverse energy cascade in a square box. *J. Fluid Mech.* **170**, 139–168.
- SOMMERIA, J. 1988 Electrically driven vortices in a strong magnetic field. *J. Fluid Mech.* **189**, 553–569.
- SOMMERIA, JOËL & MOREAU, RENÉ 1982 Why, how, and when, MHD turbulence becomes two-dimensional. *J. Fluid Mech.* **118**, 507–518, publisher: Cambridge University Press.
- STEFANI, F., FORBRIGER, J., GUNDRUM, TH., HERRMANSDÖRFER, T. & WOSNITZA, J. 2021 Mode conversion and period doubling in a liquid rubidium Alfvén-wave experiment with coinciding sound and Alfvén speeds. *Phys. Rev. Lett.* **127**, 275001.
- THOMAS, A., BASSOM, A. & DAVIES, C. 2010 Linear stability of a Stokes layer with an imposed axial magnetic field, the. *J. Fluid Mech.* **662**, 320–328.
- TIGRINE, ZAHIA, NATAF, HENRI-CLAUDE, SCHAEFFER, NATHANAËL, CARDIN, PHILIPPE & PLUNIAN, FRANCK 2019 Torsional Alfvén waves in a dipolar magnetic field: experiments and simulations. *Geophysical Journal International* **219** (Supplement\_1), S83–S100.
- TOMCZYK, S., MCINTOSH, S. W., KEIL, S. L., JUDGE, P. G., SCHAD, T., SEELEY, D. H. & EDMONDSON, J. 2007 Alfvén waves in the solar corona. *Science* **317** (5842), 1192–1196.
- TSURUTANI, BRUCE T & HO, CHRISTIAN M 1999 A review of discontinuities and Alfvén waves in interplanetary space: Ulysses results. *Reviews of Geophysics* **37** (4), 517–541.
- VARMA, ADITYA & SREENIVASAN, BINOD 2022 The role of slow magnetostrophic waves in the formation of the axial dipole in planetary dynamos. *Physics of the Earth and Planetary Interiors* **333**, 106944.
- WILCOX, JOHN M, DESILVA, ALAN W & COOPER, WILLIAM S 1961 Experiments on Alfvén-wave propagation. *Phys. Fluids* **4** (12), 1506–1513.
- WOODS, LC 1962 Hydromagnetic waves in a cylindrical plasma. *Journal of Fluid Mechanics* **13** (4), 570–586.